

¹
² Susceptible host dynamics explain pathogen resilience to
³ perturbations

⁴

⁵ **Abstract**

⁶ A major priority for epidemiological research in the time of anthropogenic change
⁷ is understanding how infectious disease dynamics respond to perturbations. Inter-
⁸ ventions to slow the spread of SARS-CoV-2 significantly disrupted the transmission
⁹ of other human pathogens. As interventions lifted, whether and when respiratory
¹⁰ pathogens would eventually return to their pre-pandemic dynamics remains to be
¹¹ answered. Here, we present a framework for estimating pathogen resilience based
¹² on how fast epidemic patterns approach their pre-pandemic, endemic dynamics and
¹³ analyze time series data from Hong Kong, Canada, Korea, and the US. By quanti-
¹⁴ fying the resilience of common respiratory pathogens, we are able to predict when
¹⁵ each pathogen will eventually return to pre-pandemic dynamics. Our predictions
¹⁶ closely match the observed deviations (or lack thereof) from its pre-COVID dynam-
¹⁷ ics. Discrepancies between predicted and observed dynamics indicate the long-term
¹⁸ impacts of pandemic perturbations, suggesting that some pathogens may be con-
¹⁹ verging to a different endemic cycle. Finally, we show that the replenishment rate
²⁰ of the susceptible pool is a key determinant of pathogen resilience, which in turn
²¹ determines the sensitivity of a system to stochastic perturbations. Overall, our anal-
²² ysis highlights the persistent nature of common respiratory pathogens compared to
²³ vaccine-preventable infections, such as measles.

24 Non-pharmaceutical interventions to slow the spread of SARS-CoV-2 disrupted
 25 the transmission of other human respiratory pathogens, adding uncertainties to their
 26 future epidemic dynamics and their public health burden [1]. As interventions lifted,
 27 large heterogeneities in outbreak dynamics were observed across different pathogens
 28 in different countries, with some pathogens exhibiting earlier and faster resurgences
 29 than others [2, 3, 4]. Heterogeneities in the overall reduction in transmission and the
 30 timing of re-emergence likely reflect differences in intervention patterns, pathogen
 31 characteristics, immigration/importation from other countries, and pre-pandemic
 32 pathogen dynamics [5]. Therefore, comparing the differential impact of the pan-
 33 demic perturbations across pathogens can provide unique opportunities to learn
 34 about underlying pathogen characteristics, such as their transmissibility or duration
 35 of immunity, from heterogeneities in re-emergence patterns [6].

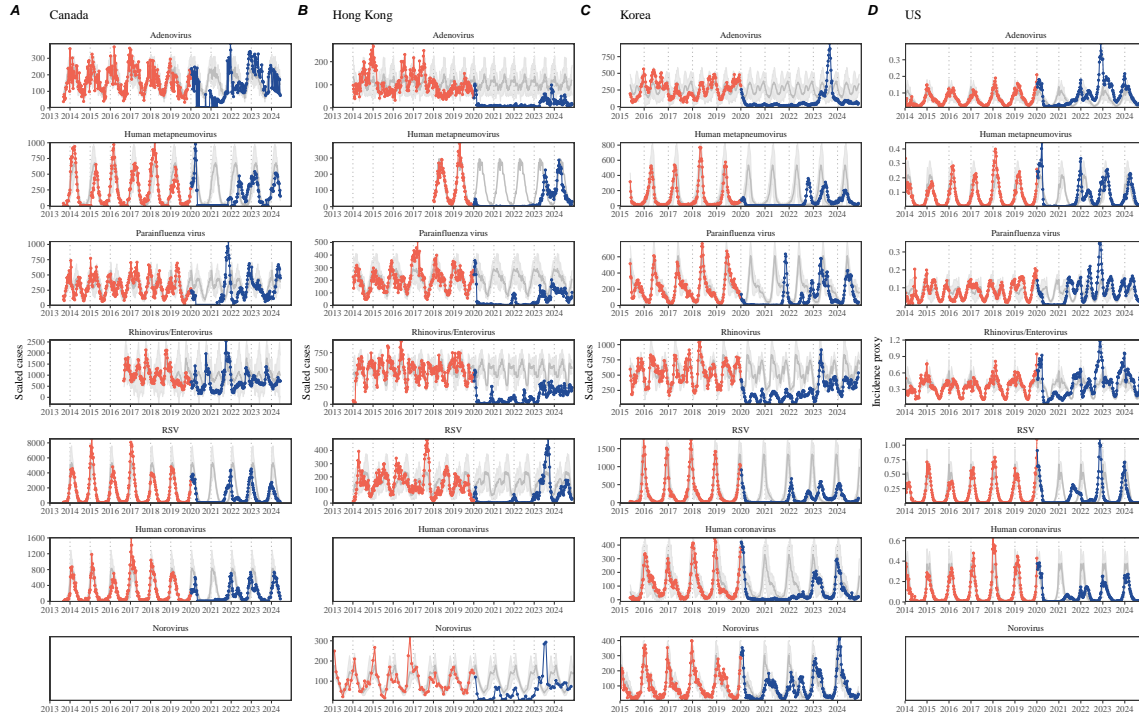


Figure 1: Observed heterogeneity in responses to pandemic perturbations across respiratory pathogens and norovirus in (A) Canada, (B) Hong Kong, (C) Korea, and (D) US. Red points and lines represent data before 2020. Blue points and lines represent data since 2020. Gray lines and shaded regions represent the mean seasonal patterns and corresponding 95% confidence intervals around the mean. Mean seasonal patterns were calculated by aggregating cases before 2020 into 52 weekly bins and taking the average in each week. Cases were scaled to account for changes in testing patterns (Materials and Methods).

36 Even though more than five years have passed since the emergence of SARS-CoV-
 37 2, we still observe persistent changes in pathogen dynamics following the pandemic

38 perturbations. For example, compared to pre-pandemic, seasonal patterns, human
39 metapneumovirus in Korea seems to circulate at lower levels, whereas RSV in Korea
40 seems to exhibit different seasonality (Figure 1). These observations suggest a funda-
41 mental change in pathogen dynamics following the pandemic perturbations, which
42 might be driven by a long-term shift in either human behavior or population-level
43 immunity [7, 8]. For example, the emergence of SARS-CoV-2 could have caused
44 a long-term shift in population-level immunity through its interactions with other
45 pathogens [9], especially with seasonal coronaviruses [7, 10, 11]. The possibility of a
46 long-lasting impact of the pandemic perturbations poses an important question for
47 future infectious disease dynamics: can we predict whether and when other pathogens
48 will eventually return to their pre-pandemic dynamics?

49 So far, most analyses of respiratory pathogens after pandemic perturbations have
50 focused on characterizing the timing of rebound [1, 12, 5]. Instead, we seek to char-
51 acterize how fast (and whether) a pathogen returns to its pre-pandemic dynamics.
52 These two concepts have a subtle but important difference. For example, it took
53 more than 3 years for human metapneumovirus to rebound in Hong Kong, but the
54 observed epidemic patterns in 2024 are similar to pre-pandemic seasonal means, sug-
55 gesting a rapid return to pre-pandemic dynamics (Figure 1). Measuring this rate of
56 return is useful because it allows us to quantify the ecological resilience of a host-
57 pathogen system, which can inform responses to future interventions [13, 14, 15, 16].

58 In this study, we lay out theoretical and statistical approaches to characterizing
59 the resilience of a host-pathogen system based on how fast the system recovers from
60 perturbation. We begin by laying out a few representative scenarios that capture
61 the potential impact of pandemic perturbations on endemic pathogen dynamics and
62 illustrate how resilience can be measured by comparing the pre- and post-pandemic
63 dynamics of susceptible and infected hosts. In practice, information on suscepti-
64 ble hosts is often unavailable, making this theoretical approach infeasible. Instead,
65 we utilize a mathematical technique to reconstruct empirical attractors from the
66 data [17], which allows us to measure the rate at which the host-pathogen system
67 approaches this empirical attractor after a perturbation; we define this rate to be
68 the empirical resilience of the host-pathogen system. We use this method to ana-
69 lyze pathogen surveillance data for respiratory and non-respiratory pathogens from
70 Canada, Hong Kong, Korea, and the US. Finally, we show that susceptible host dy-
71 namics explain variation in pathogen resilience and further demonstrate that more
72 resilient pathogens will be less sensitive to perturbations caused by demographic
73 stochasticity, thereby providing a direct link between pathogen resilience and persis-
74 tence.

75 **Conceptual introduction to pathogen resilience**

76 In classical ecological literature, the resilience of an ecological system is measured by
77 the rate at which the system returns to its reference state following a perturbation

[13, 14, 15, 16]. This rate corresponds to the largest real part of the eigenvalues of the linearized system near equilibrium—here, we refer to this value as the *intrinsic* resilience of the system, which represents the expected rate of return from perturbed states. In practice, we rarely know the true model describing population-level dynamics of common respiratory pathogens, limiting our ability to infer the intrinsic resilience of a system. Instead, we can measure the *empirical* resilience of a host-pathogen system by looking at how fast the system returns to the pre-pandemic, endemic dynamics after pandemic perturbations are lifted.

As an example, we begin with a simple Susceptible-Infected-Recovered-Susceptible (SIRS) model with seasonally forced transmission and demography (i.e., birth and death). The SIRS model is the simplest model that allows for the waning of immunity and is commonly used for modeling the dynamics of respiratory pathogens [18]. First, consider a pandemic perturbation that reduces transmission by 50% for 6 months starting in 2020, which causes epidemic patterns to deviate from their original stable annual cycle for a short period of time and eventually come back (Figure 2A). To measure the resilience of this system empirically, we first need to be able to measure the distance from its pre-pandemic attractor. There are many ways we can measure the distance from the attractor, but for illustrative purposes, we choose one of the most parsimonious approaches: that is, we look at how the susceptible (S) and infected (I) populations change over time and measure the Euclidean distance on the SI phase plane, using the unperturbed phase plane as a reference (Figure 2B; Materials and Methods). In this simple case, the locally estimated scatterplot smoothing (LOESS) fit indicates that the distance from the attractor decreases exponentially (linearly on a log scale) on average (Figure 2C). Furthermore, the overall rate of return approximates the intrinsic resilience of the seasonally unforced system (Figure 2C).

Alternatively, pandemic perturbations can have a lasting impact on the pathogen dynamics; as an example, we consider a scenario in which a 10% reduction in transmission persists even after the major pandemic perturbations are lifted (Figure 2D–F). In such cases, we cannot know whether the pathogen will return to its original cycle or a different cycle until many years have passed, and we cannot measure the distance to the new unknown attractor that the system might eventually approach. Nonetheless, we can still measure the distance from the pre-pandemic attractor and ask how the distance changes over time (Figure 2E). The LOESS fit suggests that the distance from the pre-pandemic attractor will initially decrease exponentially on average (equivalently, linearly on a log scale) and eventually plateau (Figure 2F). Here, a permanent 10% reduction in transmission rate slows the system, which causes the distance from the pre-pandemic attractor initially to decrease at a slower rate (Figure 2F) than it would have otherwise (Figure 2C) before plateauing at a fixed distance between the two attractors. This example shows that resilience is not necessarily an intrinsic property of a specific pathogen. Instead, pathogen resilience is a property of a specific attractor that a host-pathogen system approaches, which depends on both pathogen and host characteristics.

121 Finally, transient phenomena can further complicate the picture (Figure 2G–I).
122 For example, a stage-structured model, which accounts for reduction in secondary
123 susceptibility, initially exhibits a stable annual cycle, but perturbations from a 10%
124 reduction in transmission for 6 months cause the epidemic to shift to biennial cycles
125 (Figure 2G). The system eventually approaches the original pre-pandemic attractor
126 (Figure 2H), suggesting that this biennial cycle is a transient phenomenon. The
127 LOESS fit indicates that the distance from the attractor initially decreases expo-
128 nentially at a rate that is consistent with the intrinsic resilience of the seasonally
129 unforced stage-structured system, but the approach to the attractor slows down
130 with the damped oscillations (Figure 2I). This behavior is also referred to as a ghost
131 attractor, which causes long transient dynamics and slow transitions [19]. Strong
132 seasonal forcing in transmission can also lead to transient phenomena for a simple
133 SIRS model, causing a slow return to pre-perturbation dynamics (Supplementary
134 Figure S1).

135 This empirical approach allows us to measure the resilience of a two-strain host-
136 pathogen system as well even when we have incomplete observation of the infection
137 dynamics. Simulations from a simple two-strain competition system illustrate that
138 separate analyses of individual strain dynamics (e.g., RSV A vs B) and a joint anal-
139 ysis of total infections (e.g., total RSV infections) yield identical resilience estimates
140 (Supplementary Figure S2, 3). This is expected because eigenvalues determine the
141 dynamics of the entire system around the equilibrium, meaning that both strains
142 should exhibit identical rates of return following a perturbation. Analogous to a
143 single-strain system, strong seasonal forcing in transmission can cause the two-strain
144 system to slow down through transient phenomena (Supplementary Figure S4).

145 These observations yield three insights. First, we can directly estimate the em-
146 pirical resilience of a host-pathogen system by measuring the rate at which the system
147 approaches an attractor, provided that we have a way to quantify the distance from
148 the attractor. The empirical approach to estimating pathogen resilience is partic-
149 ularly convenient because it does not require us to know the true underlying model;
150 estimating the intrinsic resilience from fitting misspecified models can lead to biased
151 estimates (Supplementary Figure S5). Second, resilience estimates allow us to make
152 phenomenological predictions about the dynamics of a host-pathogen system follow-
153 ing a perturbation. Assuming that an attractor has not changed and the distance
154 from the attractor will decrease exponentially over time, we can estimate when the
155 system should reach an attractor. Finally, a change in the (exponential) rate of
156 approach provide information about whether the system has reached an alterna-
157 tive attractor, or a ghost attractor, that is different from the original, pre-pandemic
158 attractor. These alternative attractors may reflect continued perturbations from per-
159 manent changes in transmission patterns as well as changes in immune landscapes.
160 There will be periods of time when it is difficult to tell whether pathogen dynamics
161 are still diverging from the original attractor due to a long-term perturbation, or
162 have entered the basin of attraction of a new attractor; now that several years have
163 passed since interventions have been lifted, we expect many respiratory pathogens

164 to have had sufficient time to begin returning to their post-intervention attractors.
165 With recent data, we can start to evaluate whether we see early signs of convergence
166 to the former attractor or a new one.

167 Inferring pathogen resilience from real data

168 Based on these observations, we now lay out our approach to estimating pathogen
169 resilience from real data (Figure 3). We first tested this approach against simulations
170 and applied it to real data. Specifically, we analyzed case time series of respiratory
171 pathogens from four countries: Canada, Hong Kong, Korea, and the US.

172 So far, we have focused on simple examples that assume a constant transmission
173 reduction during the pandemic. However, in practice, the impact of pandemic per-
174 turbations on pathogen transmission was likely more complex (Figure 3A), reflecting
175 introduction and relaxation of various intervention strategies. In some cases, strong
176 perturbations likely caused local fadeouts, requiring immigration/importation from
177 another location for epidemic rebound. Such complexities could lead to longer de-
178lays between the introduction of pandemic perturbations and pathogen rebound as
179 well as temporal variation in outbreak sizes (Figure 3B): in this example, continued
180 transmission reduction from interventions limits the size of the first outbreak in 2021
181 following the rebound, allowing for a larger outbreak in 2022 when interventions are
182 further relaxed.

183 Previously, we relied on the dynamics of susceptible and infected hosts to com-
184pute the distance from the attractor (Figure 2), but information on susceptible hosts
185is rarely available in practice. In addition, uncertainties in case counts due to ob-
186servation error, strain evolution, and multiannual cycles in the observed epidemic
187dynamics (e.g., adenovirus circulation patterns in Hong Kong and Korea) add chal-
188lenges to defining pre-pandemic attractors, which limits our ability to measure the
189distance from the attractor. To address these challenges, we can reconstruct an em-
190pirical attractor by utilizing Takens' theorem [17], which states that an attractor of a
191nonlinear multidimensional system can be mapped onto a delayed embedding (Mate-
192rials and Methods). For example, we can use delayed logged values of pre-pandemic
193cases $C(t)$ (Figure 3C) to reconstruct the attractor:

$$\langle \log(C(t) + 1), \log(C(t - \tau) + 1), \dots, \log(C(t - (M - 1)\tau) + 1) \rangle, \quad (1)$$

194 where the delay τ and embedding dimension M are determined based on autocor-
195relations and false nearest neighbors, respectively [20, 21]. We can then apply the
196same delay and embedding dimensions to the entire time series to determine the po-
197sition in multi-dimensional state space (Figure 3D), which allows us to measure the
198nearest neighbor distance between the current state of the system and the empirical
199pre-pandemic attractor (Figure 3E). In theory, we can now quantify how fast this
200distance decreases by fitting a linear regression on a log scale, where the slope of
201the linear regression empirically measures pathogen resilience. However, resulting

estimates of pathogen resilience can be sensitive to choices about embedding delays and dimensions. For example, using longer delays and higher dimensions tends to smooth out temporal variations in the distance from the attractor (Supplementary Figure S6).

Complex changes in the distance from the attractor suggest that estimating pathogen resilience from linear regression will be particularly sensitive to our choice of fitting windows for the regression (Figure 3E). Therefore, before we tried estimating resilience from real data, we explored an automated window selection criterion for linear regression and tested it against randomized, stochastic simulations across a range of realistic pandemic perturbation shapes. In doing so, we also explored optimal choices for embedding dimensions and evaluated our choices of fitting window parameters and embedding dimensions by quantifying correlation coefficients between the estimated resilience and the intrinsic resilience of a seasonally unforced system (Materials and Methods). Overall, we found large variation in estimation performances with correlation coefficient ranging from 0.21 to 0.61 (Supplementary Figure S7). In almost all cases, the automated window selection approach outperformed a naive approach, which performs regression between the peak distance and current distance (Supplementary Figure S7).

Based on the best performing window selection criteria and embedding dimension, we applied this approach to pathogen surveillance data presented in Figure 1 (Materials and Methods). For each time series, we applied Takens' theorem independently to reconstruct the empirical attractor and obtained the corresponding time series of distances from attractors (Supplementary Figure S8). Then, we used the automated window selection criterion to fit a linear regression and estimated the empirical resilience for each pathogen in each country (Supplementary Figure S8); the window selection criterion gave poor regression window for three cases (norovirus in Hong Kong and Korea and rhinovirus/enterovirus in the US), leading to unrealistically low resilience estimates, and so we used ad-hoc regression windows instead (Supplementary Figure S9; Materials and Methods).

For all pathogens we considered, resilience estimates fell between 0.4/year and 1.8/year (Figure 4A). We estimated the mean resilience of common respiratory pathogens to be 0.99/year (95% CI: 0.81/year–1.18/year). For reference, this is \approx 7.5 times higher than the intrinsic resilience of pre-vaccination measles in England and Wales (\approx 0.13/year). Finally, resilience estimates for norovirus were comparable to those of common respiratory pathogens: 1.44/year (95%CI: 1.01/year–1.87/year) for Hong Kong and 1.07/year (95%CI: 0.86/year–1.29/year) for Korea. Based on a simple ANOVA test, we did not find significant differences in resilience estimates across countries ($p = 0.25$) or pathogens ($p = 0.67$).

Using resilience estimates, we predicted when each pathogen would hypothetically return to their pre-pandemic dynamics, assuming no long-term change in the attractor. Specifically, we extended our linear regression fits to distance-from-attractor time series and ask when the predicted regression line will cross a threshold value; since we relied on nearest neighbor distances, pre-pandemic distances are always

245 greater than zero (Figure 3E), meaning that we can use the mean of pre-pandemic
246 distances as our threshold.

247 We predicted that a return to pre-pandemic cycles has occurred or would be
248 imminent for most pathogens (Figure 4B). In particular, we predicted that 12 out
249 of 23 pathogen-country pairs should have already returned before the end of 2024.
250 For almost all pathogens that were predicted to have returned already, the observed
251 epidemic dynamics showed clear convergence towards their pre-pandemic seasonal
252 averages, confirming our predictions (Figure 4C). However, there were a few ex-
253 ceptions, including norovirus in Hong Kong and rhinovirus/enterovirus in the US,
254 where the observed epidemic dynamics in 2024 exhibit clear deviation from their pre-
255 pandemic seasonal averages (Figure 4C; Figure S9). These observations suggest a
256 possibility that some common respiratory pathogens may have converged to different
257 attractors or are still exhibiting non-equilibrium dynamics. In contrast, pathogens
258 that were predicted to have not returned yet also showed clear differences from their
259 pre-pandemic seasonal averages; as many of these pathogens are predicted to return
260 in 2025–2026, we may be able to test these predictions in near future (Supplementary
261 Figure S10). Our reconstructions of distance time series and estimates of pathogen
262 resilience and expected return time were generally robust to choices of embedding
263 dimensions (Supplementary Figure S11–12).

264 **Susceptible host dynamics explain variation in pathogen 265 resilience**

266 So far, we have focused on quantifying pathogen resilience from the observed pat-
267 terns of pathogen re-emergence following pandemic perturbations. But what factors
268 determine how resilient a host-pathogen system is? To address this question, we used
269 the SIRS model to explore how changes in susceptible host dynamics affect pathogen
270 resilience. To do so, we varied the basic reproduction number \mathcal{R}_0 , which represents
271 the average number of secondary infections caused by a newly infected individual in
272 a fully susceptible population, and the duration of immunity and computed intrinsic
273 resilience for each parameter.

274 We found that an increase in \mathcal{R}_0 and a decrease in the duration of immunity
275 correspond to an increase in pathogen resilience (Figure 5A). Similarly, an increase
276 in \mathcal{R}_0 and a decrease in the duration of immunity corresponds to a faster per-capita
277 rate of susceptible replenishment, which is defined as the ratio between absolute
278 rate at which new susceptibles enter the population and the equilibrium number of
279 susceptible individuals in the population, S^* (Figure 5B). We note that a higher \mathcal{R}_0
280 drives a faster per-capita susceptible replenishment rate by decreasing the susceptible
281 proportion at equilibrium, S^* . For a simple SIR model that assumes a life-long
282 immunity, we can show analytically that pathogen resilience is proportional to the
283 per-capita rate of susceptible replenishment (Materials and Methods). Overall, these
284 observations suggest that a faster per-capita susceptible replenishment rate causes

285 the system to be more resilient.

286 By taking the average values of empirical resilience values for each pathogen, we
287 were able to map each pathogen onto a set of parameters of the SIRS model that are
288 consistent with corresponding resilience estimates (Figure 5A). Across all pathogens
289 we considered, we estimated that the average duration of immunity is likely to be
290 short (< 4 years) across a plausible range of \mathcal{R}_0 (< 6). We were also able to obtain
291 a plausible range of susceptible replenishment rates for each pathogen (Figure 5B),
292 but there was a large uncertainty in the estimates for susceptible replenishment rates
293 due to a lack of one-to-one correspondence between susceptible replenishment rates
294 and pathogen resilience.

295 **Pathogen resilience determines sensitivity to stochastic perturbations**

296

297 Even in the absence of major pandemic perturbations, host-pathogen systems are
298 expected to experience continued perturbations of varying degrees from changes in
299 epidemiological conditions, such as human behavior, climate, and viral evolution.
300 These perturbations can also arise from demographic stochasticity, which is inherent
301 to any ecological systems. Here, we used a seasonally unforced SIRS model
302 with birth/death to explore how resilience of a host-pathogen system determines
303 the sensitivity to perturbations caused by demographic stochasticity (Materials and
304 Methods).

305 We found that resilience of a host-pathogen system determines the amount of deviation
306 from the deterministic trajectory caused by demographic stochasticity, with
307 less resilient systems experiencing larger deviations (Figure 6). Notably, less resilient
308 systems also exhibited slower epidemic cycles (Figure 6A–C). The periodicity of this
309 epidemic cycle matched those predicted by the intrinsic periodicity of the system
310 (Supplementary Figure S13) where the intrinsic resilience of the system is inversely
311 proportional to its intrinsic periodicity (Supplementary Figure S14). However, we
312 note that the interplay between seasonal transmission and intrinsic periodicity can
313 also lead to complex cycles, as illustrated by a recent analysis of *Mycoplasma pneumoniae*
314 dynamics [22].

315 We also note that the intrinsic resilience is not the sole determinant for how sensitive
316 the system is to stochastic perturbations. For example, the population size
317 and average duration of infection also affect the amount of deviation from the deter-
318 ministic trajectory caused by demographic stochasticity, even though these quantities
319 have little to no impact on the intrinsic resilience (Supplementary Figure S15). These
320 conclusions were robust for the seasonally forced SIRS model (Supplementary Figure
321 S16).

322 **Discussion**

323 COVID-19 pandemic interventions caused major disruptions to circulation patterns
324 of both respiratory and non-respiratory pathogens, adding challenges to predicting
325 their future dynamics [1, 2, 3, 4]. However, these perturbations offer large-scale natural
326 experiments for understanding how different pathogens respond to perturbations.
327 In this study, we showed that pathogen re-emergence patterns following pandemic
328 perturbations can be characterized through the lens of ecological resilience. We
329 showed that variation in pathogen resilience can be explained by the differences in
330 susceptible host dynamics, where faster replenishment of the susceptible pool corre-
331 sponds to a more resilient host-pathogen system. Finally, we showed that pathogen
332 resilience also determines the sensitivity to stochastic perturbations.

333 We analyzed case time series of common respiratory infections and norovirus
334 infections from Canada, Hong Kong, Korea, and the US to estimate their resilience.
335 Overall, we estimated the resilience of these pathogens to range from 0.4/year to
336 1.8/year, which is 3–14 times more resilient than prevaccination measles. These
337 resilience estimates indicate that common respiratory pathogens and norovirus likely
338 exhibit faster susceptible replenishment and are therefore more persistent, indicating
339 potential challenges in controlling these pathogens.

340 Based on our resilience estimates, we made phenomenological predictions about
341 when each pathogen will return to their endemic cycles. For the most part, we
342 accurately predicted which pathogens should have already returned before the end
343 of 2024. However, there were two main exceptions (i.e., norovirus in Hong Kong
344 and rhinovirus/enterovirus in the US), suggesting that these pathogens may be con-
345 verging to new endemic cycles or experiencing long-term transient behavior. These
346 changes may reflect changes in surveillance or actual shift in the dynamics, caused
347 by permanent changes in behavior or population-level immunity. While it may seem
348 unlikely that permanent changes in behavior would only affect a few pathogens and
349 not others, we cannot rule out this possibility given differences in the observed mean
350 age of infections and therefore the differences in age groups that primarily drive
351 transmission [23, 24]. Differences in the mode of transmission between respiratory
352 vs gastrointestinal pathogens may also contribute to the differences in responses to
353 pandemic perturbations.

354 For almost half of the pathogens we considered, we predicted that their return
355 to original epidemic patterns is imminent. We will need a few more years of data
356 to test whether these pathogens will eventually return to their original dynamics or
357 eventually converge to a different attractor. We also cannot rule out the possibility
358 that some pathogens may exhibit long-term transient behaviors following pandemic
359 perturbations. Overall, these observations echo earlier studies that highlighted the
360 long-lasting impact of pandemic perturbations [8, 25, 26, 4, 22].

361 We showed that susceptible host dynamics shape pathogen resilience, where faster
362 replenishment of the susceptible population causes the pathogen to be more resilient.
363 For simplicity, we focused on waning immunity and birth as the main drivers of the

364 susceptible host dynamics but other mechanisms can also contribute to the replenish-
365 ment of the susceptible population. In particular, pathogen evolution, especially the
366 emergence of antigenically novel strains, can cause effective waning of immunity in
367 the population; therefore, we hypothesize that the rate of antigenic evolution is likely
368 a key feature of pathogen resilience. Future studies should explore the relationship
369 between the rate of evolution and resilience for antigenically evolving pathogens.

370 Quantifying pathogen resilience also offers novel approaches to validating population-
371 level epidemiological models. So far, most model validation in infectious disease ecol-
372 ogy is based on the ability of a model to reproduce the observed epidemic dynamics
373 and to predict future dynamics [27, 28, 29, 30, 31]. However, many models can
374 perform similarly under these criteria. For example, two major RSV models have
375 been proposed to explain biennial epidemic patterns: (1) a stage- and age-structured
376 model that allows disease severity to vary with number of past infections and age of
377 infection [29] and (2) a pathogen-interaction model that accounts for cross immunity
378 between RSV and human metapneumovirus [28]. Since both models can accurately
379 reproduce the observed epidemic patterns, standard criteria for model validation
380 do not allow us to distinguish between these two models from population-level data
381 alone. Instead, it would be possible to measure the empirical resilience of each model
382 by simulating various perturbations and comparing the simulations to estimates of
383 empirical resilience from data, using pandemic perturbations as a reference.

384 There are several limitations to our work. First, we did not extensively explore
385 other approaches to reconstructing the attractor. Recent studies showed that more
386 sophisticated approaches, such as using non-uniform embedding, can provide more
387 robust reconstruction for noisy data [21]. In the context of causal inference, choices
388 about embedding can have major impact on the resulting inference [32]. Our re-
389 silience estimates are likely overly confident given a lack of uncertainties in attractor
390 reconstruction as well as the simplicity of our statistical framework. Nonetheless,
391 as illustrated in our sensitivity analyses, inferences about pathogen resilience in our
392 SIRS model appear to be robust to decisions about embedding lags and dimensions—
393 this is because tracking the rate at which the system approaches the attractor is likely
394 a much simpler problem than making inferences about causal directionality. Short
395 pre-pandemic time series also limit our ability to accurately reconstruct the attrac-
396 tor and contribute to the crudeness of our resilience estimates; although this is less
397 likely a problem for respiratory pathogens that are strongly annual, our attractor
398 reconstruction may be inaccurate for those exhibiting multi-annual cycles, such as
399 adenovirus in Hong Kong and Korea. Our framework also do not allow us to distin-
400 guish whether a system has settled to a new attractor or is experiencing long-term
401 transient behavior. Uncertainties in pathogen dynamics due to changes in testing
402 patterns further contribute to the crudeness of our resilience estimates. Despite these
403 limitations, our qualitative prediction that common respiratory pathogens are more
404 resilient than prevaccination measles is also likely to be robust, given how rapidly
405 many respiratory pathogens returned to their original cycles following pandemic per-
406 turbations.

407 Predicting the impact of anthropogenic changes on infectious disease dynamics
408 is a fundamental aim of infectious disease research in a rapidly changing world. Our
409 study illustrates that how a host-pathogen system responds to both small and large
410 perturbations is largely predictable through the lens of ecological resilience. In par-
411 ticular, quantifying the resilience of a host-pathogen system offers a unique insight
412 into questions about endemic pathogens' responses to pandemic perturbations, in-
413 cluding whether some pathogens will exhibit long-lasting impact from the pandemic
414 perturbation or not. More broadly, a detailed understanding of the determinants of
415 pathogen resilience can provide deeper understanding of pathogen persistence.

416 Materials and Methods

417 Data

418 We gathered time series on respiratory infections from Canada, Hong Kong, Korea,
419 and United States (US). As a reference, we also included time series data on norovirus
420 infections when available. In contrast to respiratory pathogens, we hypothesized
421 gastrointestinal viruses, such as norovirus, to be differently affected by pandemic
422 perturbations.

423 Weekly time series of respiratory infection cases in Canada came from a publicly
424 available website by the Respiratory Virus Detection Surveillance System, which
425 collects data from select laboratories across Canada [33]. Weekly time series of
426 respiratory infection cases in Hong Kong came from a publicly available website by
427 the Centre for Health Protection, Department of Health [34, 35]. Weekly time series
428 of acute respiratory infection cases in Korea came from a publicly available website
429 by the Korea Disease Control and Prevention Agency [36]. Finally, weekly time series
430 of respiratory infection cases in the US were obtained from the National Respiratory
431 and Enteric Virus Surveillance System. Time series on number of tests were also
432 available in Canada, Hong Kong, and the US, but not in Korea.

433 Data processing

434 For all time series, we rounded every year to 52 weeks by taking the average number
435 of cases and tests between the 52nd and 53rd week. We also rescale all time series to
436 account for changes in testing patterns, which were then used for the actual analysis.

437 For Canada, an increase in testing was observed from 2013 to 2024 (Supplemen-
438 tary Figure S17). To account for this increase, we calculated a 2 year moving average
439 for the number of tests for each pathogen, which we used as a proxy for testing effort.
440 Then, we divided the smoothed testing patterns by the smoothed value at the final
441 week such that the testing effort has a maximum of 1. We then divided weekly cases
442 by the testing effort to obtain a scaled case time series. A similar approach was used
443 earlier for an analysis of RSV time series in the US to account for changes in testing
444 patterns [29].

445 For Hong Kong, we applied the same scaling procedure to the time series as we
446 did for Canada. In this case, we only adjusted for testing efforts up to the end of 2019
447 because there was a major reduction in testing for common respiratory pathogens
448 between 2020 and 2023 (Supplementary Figure S18).

449 For Korea, while we did not have information on testing, the reported number
450 of respiratory infections consistently increased from 2013 to the end of 2019, which
451 we interpreted as changes in testing patterns (Supplementary Figure S19). Since
452 we did not have testing numbers, we used the weekly sum of all acute respiratory
453 viral infection cases as a proxy for testing, which were further smoothed with moving
454 average and scaled to have a maximum of 1. For Korea, we also only adjusted for
455 testing efforts up to the end of 2019.

456 In the US, there has been a large increase in testing for some respiratory pathogens,
457 especially RSV, which could not be corrected by simple scaling (Supplementary Fig-
458 ure S20). Instead, we derived an incidence proxy by multiplying the test positivity
459 with influenza-like illness positivity, which was taken from <https://gis.cdc.gov/grasp/fluvie...>. This method of estimating an inci-
460 dence proxy has been recently applied in the analysis of seasonal coronaviruses [7]
461 and *Mycoplasma pneumoniae* infections [4]. Detailed assumptions and justifications
462 are provided in [37].

464 Data summary

465 To make qualitative comparisons between pre- and post-perturbation dynamics of
466 respiratory pathogen circulation patterns, we calculated the mean seasonal patterns
467 using time series of either rescaled cases or incidence proxy estimates before 2020. We
468 did so by taking the mean value in each week across all years before 2020. Confidence
469 intervals around the means were calculated using a simple t test.

470 Estimating pathogen resilience

471 In order to measure pathogen resilience from surveillance data, we first reconstructed
472 the empirical pre-pandemic attractor of the system using Takens' embedding theorem
473 [17]. Specifically, for a given pathogen, we took the pre-pandemic (before 2020) case
474 time series $C(t)$ and reconstructed the attractor using delayed embedding with a
475 uniform delay of τ and dimension M :

$$X_{\tau,m}(t) = \langle \log(C(t) + 1), \log(C(t - \tau) + 1), \dots, \log(C(t - (M - 1)\tau) + 1) \rangle. \quad (2)$$

476 Here, the delay τ was determined by calculating the autocorrelation of the logged
477 pre-pandemic time series and asking when the autocorrelation crosses 0 for the first
478 time [21]; a typical delay for an annual outbreak is around 13 weeks.

479 Then, for a given delay τ , we determined the embedding dimension M using the
480 false nearest neighbors approach [20, 21]. To do so, we started with an embedding
481 dimension e and constructed a set of points $A_{\tau,e} = \{X_{\tau,e}(t) | t < 2020\}$. Then, for

482 each point $X_{\tau,e}(t)$, we determined the nearest neighbor from the set $A_{\tau,e}$, which we
 483 denote $X_{\tau,e}(t_{nn})$ for $t \neq t_{nn}$. Then, if the distance between these two points in the
 484 $e+1$ dimension, $D_{\tau,e+1}(t) = \|X_{\tau,e+1}(t_{nn}) - X_{\tau,e+1}(t)\|_2$, is larger than their distance
 485 in the e dimension, $D_{\tau,e}(t) = \|X_{\tau,e}(t_{nn}) - X_{\tau,e}(t)\|_2$, these two points are deemed to
 486 be false nearest neighbors; specifically, we used a threshold R for the ratio between
 487 two distances $D_{\tau,e+1}(t)/D_{\tau,e}(t)$ to determine false nearest neighbors. For the main
 488 analysis, we used $R = 10$, which was chosen from a sensitivity analysis against
 489 simulated data (Supplementary Text). Once we determined the embedding lag τ
 490 and dimension M , we apply the embedding to the entire time series and calculate
 491 the nearest neighbor distance against the attractor $A_{\tau,M}$ to obtain a time series of
 492 distance from the attractor $D_{\tau,M}(t)$.

493 From a time series of distances from the attractor, we estimated pathogen re-
 494 silience by fitting a linear regression to an appropriate window. To automatically se-
 495 lect the fitting window, we began by smoothing the distance time series using locally
 496 estimated scatterplot smoothing (LOESS) to obtain $\hat{D}_{\tau,M}(t)$, where the smoothing
 497 is performed on a log scale and exponentiated afterwards. Then, we determined
 498 threshold values (T_{start} and T_{end}) for the smoothed distances and choose the fitting
 499 window based on when $\hat{D}_{\tau,M}(t)$ crosses these threshold values for the first time.
 500 These thresholds were determined by first calculating the maximum distance,

$$\max \hat{D} = \max \hat{D}_{\tau,M}(t), \quad (3)$$

501 and the mean pre-pandemic distance,

$$\hat{D}_{\text{mean}} = \frac{1}{N_{t < 2020}} \sum_{t < 2020} \hat{D}_{\tau,M}(t), \quad (4)$$

502 as a reference, and then dividing their ratios into K equal bins,

$$T_{\text{start}} = \hat{D}_{\text{mean}} \times \left(\frac{\max \hat{D}}{\hat{D}_{\text{mean}}} \right)^{(K-a)/K}, \quad (5)$$

$$T_{\text{end}} = \hat{D}_{\text{mean}} \times \left(\frac{\max \hat{D}}{\hat{D}_{\text{mean}}} \right)^{a/K}, \quad (6)$$

503 where a represents the truncation threshold. This allows us to discard the initial
 504 period during which the distance increases (from the introduction of intervention
 505 measures) and the final period during which the distance plateaus (as the system
 506 reaches an attractor). The fitting window is determined based on when the smoothed
 507 distance $\hat{D}_{\tau,M}(t)$ crosses these threshold values for the first time; then, we fit a
 508 linear regression to logged (unsmoothed) distances $\log D_{\tau,M}(t)$ using that window.
 509 Alongside the threshold R for the false nearest neighbors approach, we tested optimal
 510 choices for K and a values using simulations (Supplementary Text). We used $K = 19$
 511 and $a = 2$ throughout the paper based on the simulation results.

512 **Mathematical modeling**

513 Throughout the paper, we use a series of mathematical models to illustrate the
 514 concept of pathogen resilience and to understand the determinants of pathogen re-
 515 silience. In general, the intrinsic resilience of a given system is given by the largest
 516 real part of the eigenvalues of the linearized system at endemic equilibrium. Here, we
 517 focus on the SIRS model with demography (birth and death) and present the details
 518 of other models in Supplementary Text. The SIRS (Susceptible-Infected-Recovered-
 519 Susceptible) model is the simplest model that allows for waning of immunity, where
 520 recovered (immune) individuals are assumed to become fully susceptible after an
 521 average of $1/\delta$ time period. The dynamics of the SIRS model is described by the
 522 following set of differential equations:

$$\frac{dS}{dt} = \mu - \beta(t)SI - \mu S + \delta R \quad (7)$$

$$\frac{dI}{dt} = \beta(t)SI - (\gamma + \mu)I \quad (8)$$

$$\frac{dR}{dt} = \gamma I - (\delta + \mu)R \quad (9)$$

523 where μ represents the birth and death rates, $\beta(t)$ represents the time-varying trans-
 524 mission rate, and γ represents the recovery rate. The basic reproduction number
 525 $\mathcal{R}_0(t) = \beta(t)/(\gamma + \mu)$ is defined as the average number of secondary infections that
 526 a single infected individual would cause in a fully susceptible population at time t
 527 and measures the intrinsic transmissibility of a pathogen.

528 When we introduced the idea of pathogen resilience (Figure 2), we imposed sinu-
 529 soidal changes to the transmission rate to account for seasonal transmission,

$$\beta(t) = b_1(1 + \theta \cos(2\pi(t - \phi)))\alpha(t), \quad (10)$$

530 where b_1 represents the baseline transmission rate, θ represents the seasonal ampli-
 531 tude, and ϕ represents the seasonal offset term. Here, we also introduced an extra
 532 multiplicative term $\alpha(t)$ to account for the impact of pandemic perturbations, where
 533 $\alpha(t) < 1$ indicates transmission reduction. Figure 2A and 2B were generated assum-
 534 ing $b_1 = 3 \times (365/7 + 1/50)/\text{years}$, $\theta = 0.2$, $\phi = 0$, $\mu = 1/50/\text{years}$, $\gamma = 365/7/\text{years}$,
 535 and $\delta = 1/2/\text{years}$. Specifically, $b_1 = 3 \times (365/7 + 1/50)/\text{years}$ implies $\mathcal{R}_0 = 3$, where
 536 $(365/7 + 1/50)/\text{years}$ represent the rate of recovery. In Figure 2A, we imposed a 50%
 537 transmission reduction for 6 months from 2020:

$$\alpha(t) = \begin{cases} 0.5 & 2020 \leq t < 2020.5 \\ 1 & \text{otherwise} \end{cases} \quad (11)$$

538 In Figure 2B, we imposed a 50% transmission reduction for 6 months from 2020 and
 539 a permanent 10% reduction onward:

$$\alpha(t) = \begin{cases} 1 & t < 2020 \\ 0.5 & 2020 \leq t < 2020.5 \\ 0.9 & 2020.5 \leq t \end{cases} \quad (12)$$

540 In both scenarios, we simulated the SIRS model from the same initial conditions
541 ($S(0) = 1/\mathcal{R}_0$, $I(0) = 1 \times 10^{-6}$, and $R(0) = 1 - S(0) - I(0)$) from 1900 until 2030.

542 To measure the empirical resilience of the SIRS model (Figure 2C and 2F), we
543 computed the normalized distance between post-intervention susceptible and logged
544 infected proportions and their corresponding unperturbed values at the same time:

$$\sqrt{\left(\frac{S(t) - S_{\text{unperturbed}}(t)}{\sigma_S}\right)^2 + \left(\frac{\log I(t) - \log I_{\text{unperturbed}}(t)}{\sigma_{\log I}}\right)^2}, \quad (13)$$

545 where σ_S and $\sigma_{\log I}$ represent the standard deviation in the unperturbed susceptible
546 and logged infected proportions. The unperturbed values were obtained by simulating
547 the same SIRS model without pandemic perturbations ($\alpha = 1$). We normalized
548 the differences in susceptible and logged infected proportions to allow both quantities
549 to equally contribute to the changes in distance from the attractor. We used logged
550 prevalence, instead of absolute prevalence, in order to capture epidemic dynamics
551 in deep troughs during the intervention period. In Supplementary Materials, we
552 also compared how the degree of seasonal transmission affects empirical resilience
553 by varying θ from 0 to 0.4; when we assumed no seasonality ($\theta = 0$), we did not
554 normalize the distance because the standard deviation of pre-intervention dynamics
555 are zero.

556 We used the SIRS model to understand how underlying epidemiological parameters
557 affect pathogen resilience and determine the relationship to underlying susceptible host dynamics. For the simple SIRS model without seasonal transmission
558 ($\theta = 0$), the intrinsic resilience equals

$$-\frac{\text{Re}(\lambda)}{2} = \frac{\delta + \beta I^* + \mu}{2}. \quad (14)$$

560 Here, I^* represents the prevalence at endemic equilibrium:

$$I^* = \frac{(\delta + \mu)(\beta - (\gamma + \mu))}{\beta(\delta + \gamma + \mu)}. \quad (15)$$

561 The susceptible replenishment rate is given by

$$S_{\text{replenish}} = \frac{\mu + \delta R}{S^*}, \quad (16)$$

562 where $S^* = 1/\mathcal{R}_0$ represents the equilibrium proportion of susceptible individuals.
563 We varied the basic reproduction number \mathcal{R}_0 between 1.1 to 6 and the average
564 duration of immunity $1/\delta$ between 2 to 4 years, and computed these two quantities.
565 In doing so, we fixed all other parameters: $\mu = 1/80/\text{years}$ and $\gamma = 365/7/\text{years}$.
566 When infection provides a life-long immunity ($\delta = 0$), the intrinsic resilience is
567 inversely proportional to the susceptible replenishment rate:

$$-\frac{\text{Re}(\lambda)}{2} = \frac{\mu}{2S^*} = \frac{S_{\text{replenish}}}{2}. \quad (17)$$

Finally, we used a seasonally unforced stochastic SIRS model without demography to understand how pathogen resilience affects sensitivity of the system to demographic stochasticity (see Supplementary Text for the details of the stochastic SIRS model). By varying the basic reproduction number \mathcal{R}_0 between 2 to 20 and the average duration of immunity $1/\delta$ between 1 to 40 years, we ran the SIRS model for 100 years and computed the epidemic amplitude, which we defined as $(\max I - \min I)/(2\bar{I})$. Each simulation began from the equilibrium, and we truncated the initial 25 years before computing the epidemic amplitude. In doing so, we assumed $\gamma = 365/7/\text{years}$ and fixed the population size to 1 billion to prevent any fadeouts. We also considered a seasonally forced stochastic SIRS model without demography, assuming an amplitude of seasonal forcing of 0.04; in this case, we computed the relative epidemic amplitude by comparing the deterministic and stochastic trajectories (Supplementary Materials).

581 Data availability

All data and code are stored in a publicly available GitHub repository (<https://github.com/cobeylab/return-time>).

584 Funding

S.W.P. is a Peter and Carmen Lucia Buck Foundation Awardee of the Life Sciences Research Foundation. S.C. was supported by Federal funds from the National Institute of Allergy and Infectious Diseases, National Institutes of Health, Department of Health and Human Services under CEIRR contract 75N93021C00015. The content is solely the responsibility of the authors and does not necessarily represent the official views of the NIAID or the National Institutes of Health.

591 **Supplementary Text**

592 **Resilience of a stage-structured system.**

593 In Figure 2G–I, we used a more realistic, stage-structured model to illustrate how
 594 transient phenomena can cause the system to slow down. Specifically, we used the
 595 stage-structured RSV model proposed by [29], which assumes that subsequent rein-
 596 fections cause an individual to become less susceptible and transmissible than previ-
 597 ous infections. In contrast to a standard SIRS model, this model does not include a
 598 recovered compartment, which allow for temporary protection against new infections,
 599 and assumes that recovered individuals are immediately susceptible to new infections.
 600 The model dynamics can be described as follows:

$$\frac{dM}{dt} = \mu - (\omega + \mu)M \quad (S1)$$

$$\frac{dS_0}{dt} = \omega M - (\lambda(t) + \mu)S_0 \quad (S2)$$

$$\frac{dI_1}{dt} = \lambda(t)S_0 - (\gamma_1 + \mu)I_1 \quad (S3)$$

$$\frac{dS_1}{dt} = \gamma_1 I_1 - (\sigma_1 \lambda(t) + \mu)S_1 \quad (S4)$$

$$\frac{dI_2}{dt} = \sigma_1 \lambda(t)S_1 - (\gamma_2 + \mu)I_2 \quad (S5)$$

$$\frac{dS_2}{dt} = \gamma_2 I_2 - (\sigma_2 \lambda(t) + \mu)S_2 \quad (S6)$$

$$\frac{dI_3}{dt} = \sigma_2 \lambda(t)S_2 - (\gamma_3 + \mu)I_3 \quad (S7)$$

$$\frac{dS_3}{dt} = \gamma_3 I_3 - (\sigma_3 \lambda(t) + \mu)S_3 + \gamma_4 I_4 \quad (S8)$$

$$\frac{dI_4}{dt} = \sigma_3 \lambda(t)S_3 - (\gamma_4 + \mu)I_4 \quad (S9)$$

601 where M represents the proportion of individuals who are maternally immune; S_i
 602 represents the proportion of individuals who are susceptible after i prior infections; I_i
 603 represents the proportion of individuals who are currently (re)-infected with their i -th
 604 infection; μ represents the birth and death rates; $1/\omega$ represents the mean duration
 605 of maternal immunity; $1/\gamma_i$ represents the mean duration of infection; $\lambda(t)$ represents
 606 the force of infection; and σ_i represents the reduction in susceptibility for the i -th
 607 reinfection. The force of infection is modeled using a sinusoidal function:

$$\beta(t) = b_1(1 + \theta \cos(2\pi(t - \phi)))\alpha(t) \quad (S10)$$

$$\lambda(t) = \beta(I_1 + \rho_1 I_2 + \rho_2(I_3 + I_4)), \quad (S11)$$

608 where b_1 represents the baseline transmission rate; θ represents the seasonal ampli-
 609 tude; ϕ represents the seasonal offset term; $\alpha(t)$ represents the intervention effect;

and ρ_i represents the impact of immunity on transmission reduction. We used the following parameters to simulate the impact of interventions on epidemic dynamics [29]: $b_1 = 9 \times (365/10 + 1/80)/\text{years}$, $\theta = 0.2$, $\phi = -0.1$, $\omega = 365/112/\text{years}$, $\gamma_1 = 365/10/\text{years}$, $\gamma_2 = 365/7/\text{years}$, $\gamma_3 = 365/5/\text{years}$, $\sigma_1 = 0.76$, $\sigma_2 = 0.6$, $\sigma_3 = 0.4$, $\rho_1 = 0.75$, $\rho_2 = 0.51$, and $\mu = 1/80/\text{years}$. We assumed a 50% transmission reduction for 6 months from 2020:

$$\alpha(t) = \begin{cases} 0.5 & 2020 \leq t < 2020.5 \\ 1 & \text{otherwise} \end{cases} \quad (\text{S12})$$

The model was simulated from 1900 to 2030 using the following initial conditions: $M = 0$, $S_0 = 1/\mathcal{R}_0 - I_1$, $I_1 = 1 \times 10^{-6}$, $S_1 = 1 - 1/\mathcal{R}_0$, $I_2 = 0$, $S_2 = 0$, $I_3 = 0$, $S_3 = 0$, and $I_4 = 0$. For the phase plane analysis (Figure 2H) and distance analysis (Figure 2I), we relied on the average susceptibility,

$$\bar{S} = S_0 + \sigma_1 S_1 + \sigma_2 S_2 + \sigma_3 S_3, \quad (\text{S13})$$

and total prevalence,

$$I_{\text{total}} = I_1 + I_2 + I_3 + I_4. \quad (\text{S14})$$

These quantities were used to compute the normalized distance from the attractor, as described in the main text.

Resilience of a multistain system.

We used a simple two-strain model to show that a multistain host-pathogen system that is coupled through cross immunity can be described by a single resilience value. The model dynamics can be described as follows [28]:

$$\frac{dS}{dt} = \mu - \mu S - (\lambda_1 + \lambda_2)S + \delta_1 R_1 + \delta_2 R_2 \quad (\text{S15})$$

$$\frac{dI_1}{dt} = \lambda_1 S - (\gamma_1 + \mu)I_1 \quad (\text{S16})$$

$$\frac{dI_2}{dt} = \lambda_2 S - (\gamma_2 + \mu)I_2 \quad (\text{S17})$$

$$\frac{dR_1}{dt} = \gamma_1 I_1 - \lambda_2 \epsilon_{21} R_1 - \delta_1 R_1 + \delta_2 R - \mu R_1 \quad (\text{S18})$$

$$\frac{dR_2}{dt} = \gamma_2 I_2 - \lambda_1 \epsilon_{12} R_2 - \delta_2 R_2 + \delta_1 R - \mu R_2 \quad (\text{S19})$$

$$\frac{dJ_1}{dt} = \lambda_1 \epsilon_{12} R_2 - (\gamma_1 + \mu) J_1 \quad (\text{S20})$$

$$\frac{dJ_2}{dt} = \lambda_2 \epsilon_{21} R_1 - (\gamma_2 + \mu) J_2 \quad (\text{S21})$$

$$\frac{dR}{dt} = \gamma_1 J_1 + \gamma_2 J_2 - \delta_1 R - \delta_2 R - \mu R \quad (\text{S22})$$

where S represents the proportion of individuals who are fully susceptible to infections by both strains; I_1 represents the proportion of individuals who are infected with strain 1 without prior immunity; I_2 represents the proportion of individuals who are infected with strain 2 without prior immunity; R_1 represents the proportion of individuals who are fully immune against strain 1 and partially susceptible to reinfection by strain 2; R_2 represents the proportion of individuals who are fully immune against strain 2 and partially susceptible to reinfection by strain 1; J_1 represents the proportion of individuals who are infected with strain 1 with prior immunity against strain 2; J_2 represents the proportion of individuals who are infected with strain 2 with prior immunity against strain 1; R represents the proportion of individuals who are immune to infections from both strains; μ represents the birth/death rate; λ_1 and λ_2 represent the force of infection from strains 1 and 2, respectively; δ_1 and δ_2 represent the waning immunity rate; γ_1 and γ_2 represent the recovery rate; ϵ_{21} and ϵ_{12} represent the susceptibility to reinfection with strains 2 and 1, respectively, given prior immunity from infection with strains 1 and 2, respectively. The force of infection is modeled as follows:

$$\beta_1 = b_1(1 + \theta_1 \sin(2\pi(t - \phi_1)))\alpha(t) \quad (\text{S23})$$

$$\beta_2 = b_2(1 + \theta_2 \sin(2\pi(t - \phi_2)))\alpha(t) \quad (\text{S24})$$

$$\lambda_1 = \beta_1(I_1 + J_1) \quad (\text{S25})$$

$$\lambda_2 = \beta_2(I_2 + J_2) \quad (\text{S26})$$

In Supplementary Figures S2–S4, we assumed the following parameters: $b_1 = 2 \times 52/\text{years}$, $b_2 = 4 \times 52/\text{years}$, $\phi_1 = \phi_2 = 0$, $\epsilon_{12} = 0.9$, $\epsilon_{21} = 0.5$, $\gamma_1 = \gamma_2 = 52/\text{years}$, $\delta_1 = \delta_2 = 1/\text{years}$, and $\mu = 1/70/\text{years}$. For all simulations, we assumed a 50% transmission reduction for 6 months from 2020:

$$\alpha(t) = \begin{cases} 0.5 & 2020 \leq t < 2020.5 \\ 1 & \text{otherwise} \end{cases} \quad (\text{S27})$$

The seasonal amplitude θ is varied from 0 to 0.4. All simulations were run from 1900 to 2030 with following initial conditions: $S(0) = 1 - 2 \times 10^{-6}$, $I_1(0) = 1 \times 10^{-6}$, $I_2(0) = 1 \times 10^{-6}$, $R_1(0) = 0$, $R_2(0) = 0$, $J_1(0) = 0$, $J_2(0) = 0$, and $R(0) = 0$.

We considered three scenarios for measuring pathogen resilience: (1) we only have information about strain 1, (2) we only have information about strain 2, and (3) we are unable to distinguish between strains. In the first two scenarios (see panels A–C for strain 1 and panels D–F for strain 2), we considered the dynamics of average susceptibility for each strain and total prevalence:

$$\bar{S}_1 = S + \epsilon_{12}R_2 \quad (\text{S28})$$

$$\hat{I}_1 = I_1 + J_1 \quad (\text{S29})$$

$$\bar{S}_2 = S + \epsilon_{21}R_1 \quad (\text{S30})$$

$$\hat{I}_2 = I_2 + J_2 \quad (\text{S31})$$

655 In the third scenario (panels G–I), we considered the dynamics of total susceptible
 656 and infected populations:

$$\hat{S} = S + R_2 + R_1 \quad (\text{S32})$$

$$\hat{I} = I_1 + J_1 + I_2 + J_2 \quad (\text{S33})$$

657 These quantities were used to compute the normalized distance from the attractor,
 658 as described in the main text.

659 Estimating intrinsic resilience using a mechanistic model

660 We tested whether we can reliably estimate the intrinsic resilience of a system by fit-
 661 ting a mechanistic model. Specifically, we simulated case time series from stochastic
 662 SIRS and two-strain models and fitted a simple, deterministic SIRS model using a
 663 Bayesian framework [4, 22, 38].

664 We simulated the models in discrete time with a daily time step ($\Delta t = 1$),
 665 incorporating demographic stochasticity:

$$\beta(t) = \mathcal{R}_0 \left(1 + \theta \cos \left(\frac{2\pi t}{364} \right) \right) \alpha(t)(1 - \exp(-\gamma)) \quad (\text{S34})$$

$$\text{FOI}(t) = \beta(t)I(t - \Delta t)/N \quad (\text{S35})$$

$$B(t) \sim \text{Poisson}(\mu N) \quad (\text{S36})$$

$$\Delta S(t) \sim \text{Binom}(S(t - \Delta t), 1 - \exp(-(\text{FOI}(t) + \mu)\Delta t)) \quad (\text{S37})$$

$$N_{SI}(t) \sim \text{Binom}\left(\Delta S(t), \frac{\text{FOI}(t)}{\text{FOI}(t) + \mu}\right) \quad (\text{S38})$$

$$\Delta I(t) \sim \text{Binom}(I(t - \Delta t), 1 - \exp(-(\gamma + \mu)\Delta t)) \quad (\text{S39})$$

$$N_{IR}(t) \sim \text{Binom}\left(\Delta I(t), \frac{\gamma}{\gamma + \mu}\right) \quad (\text{S40})$$

$$\Delta R(t) \sim \text{Binom}(R(t - \Delta t), 1 - \exp(-(\delta + \mu)\Delta t)) \quad (\text{S41})$$

$$N_{RS}(t) \sim \text{Binom}\left(\Delta R(t), \frac{\delta}{\delta + \mu}\right) \quad (\text{S42})$$

$$S(t) = S(t - \Delta t) + N_{RS}(t) + B(t) - \Delta S(t) \quad (\text{S43})$$

$$I(t) = I(t - \Delta t) + N_{SI}(t) - \Delta I(t) \quad (\text{S44})$$

$$R(t) = R(t - \Delta t) + N_{IR}(t) - \Delta R(t) \quad (\text{S45})$$

666 where FOI represents the force of infection; N_{ij} represents the number of individuals
 667 moving from compartment i to j on a given day; and $B(t)$ represents the number
 668 of new births. All other parameters definitions can be found in the description of
 669 the deterministic version of the model. We simulated the model on a daily scale—
 670 assuming 364 days in a year so that it can be evenly grouped into 52 weeks—with
 671 the following parameters: $\mathcal{R}_0 = 3$, $\theta = 0.1$, $\gamma = 1/7/\text{days}$, $\delta = 1/(364 \times 2)/\text{days}$,

⁶⁷² $\mu = 1/(364 \times 50)$ /days, and $N = 1 \times 10^8$. The model was simulated from 1900 to
⁶⁷³ 2030 assuming $S(0) = N/3$, $I(0) = 100$, and $R(0) = N - S(0) - I(0)$. The observed
⁶⁷⁴ incidence from the model was then simulated as follows:

$$C(t) = \text{Beta-Binom}(N_{SI}(t), \rho, k), \quad (\text{S46})$$

⁶⁷⁵ where ρ represents the reporting probability and k represents the overdispersion
⁶⁷⁶ parameter of beta-binomial distribution. Here, we used the beta-binomial distribu-
⁶⁷⁷ tion to account for overdispersion in reporting. We assumed $\rho = 0.002$ (i.e., 0.2%
⁶⁷⁸ probability) and $k = 1000$.

⁶⁷⁹ We used an analogous approach for the two-strain model:

$$\beta_1(t) = b_1 \left(1 + \theta_1 \cos \left(\frac{2\pi(t - \phi_1)}{364} \right) \right) \alpha(t) \quad (\text{S47})$$

$$\beta_2(t) = b_2 \left(1 + \theta_2 \cos \left(\frac{2\pi(t - \phi_2)}{364} \right) \right) \alpha(t) \quad (\text{S48})$$

$$\text{FOI}_1(t) = \beta_1(t)(I_1(t - \Delta t) + J_1(t - \Delta t))/N \quad (\text{S49})$$

$$\text{FOI}_2(t) = \beta_2(t)(I_2(t - \Delta t) + J_2(t - \Delta t))/N \quad (\text{S50})$$

$$B(t) \sim \text{Poisson}(\mu N) \quad (\text{S51})$$

$$\Delta S(t) \sim \text{Binom}(S(t - \Delta t), 1 - \exp(-(\text{FOI}_1(t) + \text{FOI}_2(t) + \mu)\Delta t)) \quad (\text{S52})$$

$$N_{SI_1}(t) \sim \text{Binom}\left(\Delta S(t), \frac{\text{FOI}_1(t)}{\text{FOI}_1(t) + \text{FOI}_2(t) + \mu}\right) \quad (\text{S53})$$

$$N_{SI_2}(t) \sim \text{Binom}\left(\Delta S(t), \frac{\text{FOI}_2(t)}{\text{FOI}_1(t) + \text{FOI}_2(t) + \mu}\right) \quad (\text{S54})$$

$$\Delta I_1(t) \sim \text{Binom}(I_1(t - \Delta t), 1 - \exp(-(\gamma_1 + \mu)\Delta t)) \quad (\text{S55})$$

$$N_{I_1 R_1}(t) \sim \text{Binom}\left(\Delta I_1(t), \frac{\gamma_1}{\gamma_1 + \mu}\right) \quad (\text{S56})$$

$$\Delta I_2(t) \sim \text{Binom}(I_2(t - \Delta t), 1 - \exp(-(\gamma_2 + \mu)\Delta t)) \quad (\text{S57})$$

$$N_{I_2 R_2}(t) \sim \text{Binom}\left(\Delta I_2(t), \frac{\gamma_2}{\gamma_2 + \mu}\right) \quad (\text{S58})$$

$$\Delta R_1(t) \sim \text{Binom}(R_1(t - \Delta t), 1 - \exp(-(\epsilon_{21}\text{FOI}_2(t) + \rho_1 + \mu)\Delta t)) \quad (\text{S59})$$

$$N_{R_1 S}(t) \sim \text{Binom}\left(\Delta R_1(t), \frac{\rho_1}{\epsilon_{21}\text{FOI}_2(t) + \rho_1 + \mu}\right) \quad (\text{S60})$$

$$N_{R_1 J_2}(t) \sim \text{Binom}\left(\Delta R_1(t), \frac{\epsilon_{21}\text{FOI}_2(t)}{\epsilon_{21}\text{FOI}_2(t) + \rho_1 + \mu}\right) \quad (\text{S61})$$

$$\Delta R_2(t) \sim \text{Binom}(R_2(t - \Delta t), 1 - \exp(-(\epsilon_{12}\text{FOI}_1(t) + \rho_2 + \mu)\Delta t)) \quad (\text{S62})$$

$$N_{R_2 S}(t) \sim \text{Binom}\left(\Delta R_2(t), \frac{\rho_2}{\epsilon_{12}\text{FOI}_1(t) + \rho_2 + \mu}\right) \quad (\text{S63})$$

$$N_{R_2 J_1}(t) \sim \text{Binom}\left(\Delta R_2(t), \frac{\epsilon_{12}\text{FOI}_1(t)}{\epsilon_{12}\text{FOI}_1(t) + \rho_2 + \mu}\right) \quad (\text{S64})$$

$$\Delta J_1(t) \sim \text{Binom}(J_1(t - \Delta t), 1 - \exp(-(\gamma_1 + \mu)\Delta t)) \quad (\text{S65})$$

$$N_{J_1R}(t) \sim \text{Binom}\left(\Delta J_1(t), \frac{\gamma_1}{\gamma_1 + \mu}\right) \quad (\text{S66})$$

$$\Delta J_2(t) \sim \text{Binom}(J_2(t - \Delta t), 1 - \exp(-(\gamma_2 + \mu)\Delta t)) \quad (\text{S67})$$

$$N_{J_2R}(t) \sim \text{Binom}\left(\Delta J_2(t), \frac{\gamma_2}{\gamma_2 + \mu}\right) \quad (\text{S68})$$

$$\Delta R(t) \sim \text{Binom}(R(t - \Delta t), 1 - \exp(-(\rho_1 + \rho_2 + \mu)\Delta t)) \quad (\text{S69})$$

$$N_{RR_1}(t) \sim \text{Binom}\left(\Delta R(t), \frac{\rho_1}{\rho_1 + \rho_2 + \mu}\right) \quad (\text{S70})$$

$$N_{RR_2}(t) \sim \text{Binom}\left(\Delta R(t), \frac{\rho_2}{\rho_1 + \rho_2 + \mu}\right) \quad (\text{S71})$$

$$S(t) = S(t - \Delta t) - \Delta S(t) + B(t) + N_{R_1S}(t) + N_{R_2S}(t) \quad (\text{S72})$$

$$I_1(t) = I_1(t - \Delta t) - \Delta I_1(t) + N_{SI_1}(t) \quad (\text{S73})$$

$$I_2(t) = I_2(t - \Delta t) - \Delta I_2(t) + N_{SI_2}(t) \quad (\text{S74})$$

$$R_1(t) = R_1(t - \Delta t) - \Delta R_1(t) + N_{I_1R_1}(t) + N_{RR_1}(t) \quad (\text{S75})$$

$$R_2(t) = R_2(t - \Delta t) - \Delta R_2(t) + N_{I_2R_2}(t) + N_{RR_2}(t) \quad (\text{S76})$$

$$J_1(t) = J_1(t - \Delta t) - \Delta J_1(t) + N_{R_2J_1}(t) \quad (\text{S77})$$

$$J_2(t) = J_2(t - \Delta t) - \Delta J_2(t) + N_{R_1J_2}(t) \quad (\text{S78})$$

$$R(t) = R(t - \Delta t) - \Delta R(t) + N_{J_1R}(t) + N_{J_2R}(t) \quad (\text{S79})$$

We simulated the model on a daily scale with previously estimated parameters for the RSV-HMPV interaction [28]: $b_1 = 1.7/\text{weeks}$, $b_2 = 1.95/\text{weeks}$, $\theta_1 = 0.4$, $\theta_2 = 0.3$, $\phi_1 = 0.005 \times 7/364$, $\phi_2 = 4.99 \times 7/364$, $\epsilon_{12} = 0.92$, $\epsilon_{21} = 0.45$, $\gamma_1 = 1/10/\text{days}$, $\gamma_2 = 1/10/\text{days}$, $\rho_1 = 1/364/\text{days}$, $\rho_2 = 1/364/\text{days}$, $\mu = 1/(70 \times 364)/\text{days}$, and $N = 1 \times 10^8$. The model was simulated from 1900 to 2030 assuming $S(0) = N - 200$, $I_1(0) = 100$, $I_2(0) = 100$, $R_1(0) = 0$, $R_2(0) = 0$, $J_1(0) = 0$, $J_2(0) = 0$, and $R(0) = 0$. The observed incidence for each strain is then simulated as follows:

$$C_1(t) = \text{Beta-Binom}(N_{SI_1}(t) + N_{R_2J_1}, \rho, k), \quad (\text{S80})$$

$$C_2(t) = \text{Beta-Binom}(N_{SI_2}(t) + N_{R_1J_2}, \rho, k), \quad (\text{S81})$$

where ρ represents the reporting probability and k represents the overdispersion parameter of beta-binomial distribution. We assumed $\rho = 0.002$ (i.e., 0.2% probability) and $k = 500$. We also considered the total incidence: $C_{\text{total}}(t) = C_1(t) + C_2(t)$.

For both models, we considered a more realistically shaped pandemic perturbation $\alpha(t)$ to challenge our ability to estimate the intervention effects. Thus, we assumed a 40% transmission reduction for 3 months from March 2020, followed by a 10% transmission reduction for 6 months, 20% transmission reduction for 3 months,

694 and a final return to normal levels:

$$\alpha(t) = \begin{cases} 1 & t < 2020.25 \\ 0.6 & 2020.25 \leq t < 2020.5 \\ 0.9 & 2020.5 \leq t < 2021 \\ 0.8 & 2021 \leq t < 2021.25 \\ 1 & 2021.25 \leq t \end{cases}. \quad (\text{S82})$$

695 For all simulations, we truncated the time series from the beginning of 2014 to the
696 end of 2023 and aggregated them into weekly cases.

697 To infer intrinsic resilience from time series, we fitted a simple discrete time,
698 deterministic SIRS model in a Bayesian framework [4]:

$$\Delta t = 1 \text{ week} \quad (\text{S83})$$

$$\text{FOI}(t) = \beta(t)(I(t - \Delta t) + \omega)/N \quad (\text{S84})$$

$$\Delta S(t) = [1 - \exp(-(\text{FOI}(t) + \mu)\Delta t)] S(t - \Delta t) \quad (\text{S85})$$

$$N_{SI}(t) = \frac{\text{FOI}(t)\Delta S(t)}{\text{FOI}(t) + \mu} \quad (\text{S86})$$

$$\Delta I(t) = [1 - \exp(-(\gamma + \mu)\Delta t)] I(t - \Delta t) \quad (\text{S87})$$

$$N_{IR}(t) = \frac{\gamma \Delta I(t)}{\gamma + \mu} \quad (\text{S88})$$

$$\Delta R(t) = [1 - \exp(-(\nu + \mu)\Delta t)] R(t - \Delta t) \quad (\text{S89})$$

$$N_{RS}(t) = \frac{\nu \Delta R(t)}{\nu + \mu} \quad (\text{S90})$$

$$S(t) = S(t - \Delta t) + \mu S - \Delta S(t) + N_{RS}(t) \quad (\text{S91})$$

$$I(t) = I(t - \Delta t) - \Delta I(t) + N_{SI}(t) \quad (\text{S92})$$

$$R(t) = R(t - \Delta t) - \Delta R(t) + N_{IR}(t) \quad (\text{S93})$$

699 where we include an extra term ω to account for importation. Although actual
700 simulations did not include any importation, we had found that including this term
701 generally helped with model convergence in previous analyses [4]. The transmission
702 rate was divided into a seasonal term $\beta_{\text{seas}}(t)$ (repeated every year) and intervention
703 term $\alpha(t)$, which were estimated jointly:

$$\beta(t) = \beta_{\text{seas}}(t)\alpha(t), \quad (\text{S94})$$

704 where $\alpha < 1$ corresponds to reduction in transmission due to intervention effects. To
705 constrain the smoothness of $\beta_{\text{seas}}(t)$, we imposed cyclic, random-walk priors:

$$\beta_{\text{seas}}(t) \sim \text{Normal}(\beta_{\text{seas}}(t - 1), \sigma) \quad t = 2 \dots 52 \quad (\text{S95})$$

$$\beta_{\text{seas}}(1) \sim \text{Normal}(\beta_{\text{seas}}(52), \sigma) \quad (\text{S96})$$

706 We fixed $\alpha(t) = 1$ for all $t < 2020$ and estimate α assuming a normal prior:

$$\alpha \sim \text{Normal}(1, 0.25). \quad (\text{S97})$$

707 We assumed weakly informative priors on ω and ν :

$$\omega \sim \text{Normal}(0, 200) \quad (\text{S98})$$

$$\nu \sim \text{Normal}(104, 26) \quad (\text{S99})$$

708 We assumed that the true birth/death rates, population sizes, and recovery rates
709 are known. We note, however, that assuming $\gamma = 1/\text{week}$ actually corresponds to
710 a mean simulated infectious period of 1.6 weeks due to a time discretization, which
711 is much longer than the true value; this approximation allows us to test whether we
712 can still robustly estimate the intrinsic resilience given parameter mis-specification.
713 Initial conditions were estimated with following priors:

$$S(0) = Ns(0) \quad (\text{S100})$$

$$I(0) = Ni(0) \quad (\text{S101})$$

$$s(0) \sim \text{Uniform}(0, 1) \quad (\text{S102})$$

$$i(0) \sim \text{Half-Normal}(0, 0.001) \quad (\text{S103})$$

714 Finally, the observation model was specified as follows:

$$\text{Cases}(t) \sim \text{Negative-Binomial}(\rho N_{SI}(t), \phi) \quad (\text{S104})$$

$$\rho \sim \text{Half-Normal}(0, 0.02) \quad (\text{S105})$$

$$\phi \sim \text{Half-Normal}(0, 10) \quad (\text{S106})$$

715 where ρ represents the reporting probability and ϕ represents the negative binomial
716 overdispersion parameter.

717 The model was fitted to four separate time series: (1) incidence time series from
718 the SIRS model, (2) incidence time series for strain 1 from the two-strain model,
719 (3) incidence time series for strain 2 from the two-strain model, and (4) combined
720 incidence time series for strains 1 and 2 from the two-strain model. The model was
721 fitted using rstan [39, 40]. The resulting posterior distribution was used to calculate
722 the intrinsic resilience of the seasonally unforced system with the same parameters;
723 eigenvalues of the discrete-time SIR model were computed by numerically finding
724 the equilibrium and calculating the Jacobian matrix.

725 **Validations for window-selection criteria**

726 We used stochastic SIRS simulations to identify optimal parameters for the window-
727 selection criteria that we used for the linear regression for estimating empirical re-
728 silience. For each simulation, we began by generating a random perturbation $\alpha(t)$
729 from a random set of parameters. First, we drew the duration of perturbation τ_{np}^i

730 from a uniform distribution between 1 and 2 years. Then, we drew independent
 731 normal variables z_i of length $\lfloor 364\tau_{\text{np}} \rfloor$ with a standard deviation of 0.02 and took a
 732 reverse cumulative sum to obtain a realistic shape for the perturbation:

$$x_n = 1 + \sum_{i=n}^{\lfloor 364\tau_{\text{np}} \rfloor} z_i, \quad n = 1, \dots, \lfloor 364\tau_{\text{np}} \rfloor. \quad (\text{S107})$$

733 In contrast to simple perturbations that assume a constant reduction in transmis-
 734 sion, this approach allows us to model transmission reduction that varies over time
 735 smoothly. We repeated this random generation process until less than 10% of x_n
 736 exceeds 1—this was done to ensure the perturbation term $\alpha(t)$ stays below 1 (and
 737 therefore reduce transmission) for the most part. Then, we set any values that are
 738 above 1 or below 0 to 1 and 0, respectively. Then, we randomly drew the minimum
 739 transmission during perturbation α_{\min} from a uniform distribution between 0.5 and
 740 0.7 and scale x_n to have a minimum of α_{\min} :

$$x_{\text{scale},n} = \alpha_{\min} + (1 - \alpha_{\min}) \times \frac{x_n - \min x_n}{1 - \min x_n}. \quad (\text{S108})$$

741 This allowed us to simulate a realistically shaped perturbation:

$$\alpha(t) = \begin{cases} 1 & t < 2020 \\ x_{\text{scale},364(t-2020)} & 2020 \leq t < 2020 + \tau_{\text{np}} \\ 1 & \tau_{\text{np}} \leq t \end{cases} \quad (\text{S109})$$

742 Given this perturbation function, we draw \mathcal{R}_0 from a uniform distribution between
 743 1.5 and 4 and the mean duration of immunity $1/\delta$ from a uniform distribution be-
 744 tween 1 and 4. Then, we simulate the stochastic SIRS model from $S(0) = 10^8/\mathcal{R}_0$
 745 and $I(0) = 100$ from 1990 to 2025 and truncate the time series to 2014–2025; if the
 746 epidemic becomes extinct before the end of simulation, we discard that simulation
 747 and start over from the perturbation generation step.

748 For each epidemic simulation, we computed the empirical resilience by varying
 749 the threshold R for the nearest neighbor approach from 4 to 14 with increments of
 750 2, the number of divisions K for the window selection between 8 and 25, and the
 751 truncation threshold a for the window selection between 1 to 3; this was done for all
 752 possible combinations of R , K , and a . We also compared this with the naive approach
 753 that uses the entire distance-from-attractor time series, starting from the maximum
 754 distance to the end of the time series. We repeated this procedure 500 times and
 755 quantified the correlation between empirical and intrinsic resilience estimates across
 756 two approaches.

⁷⁵⁷ **Supplementary Figures**

758 **References**

- 759 [1] Rachel E Baker, Sang Woo Park, Wenchang Yang, Gabriel A Vecchi, C Jessica E
760 Metcalf, and Bryan T Grenfell. The impact of COVID-19 nonpharmaceutical
761 interventions on the future dynamics of endemic infections. *Proceedings of the
762 National Academy of Sciences*, 117(48):30547–30553, 2020.
- 763 [2] Gabriela B Gomez, Cedric Mahé, and Sandra S Chaves. Uncertain effects of the
764 pandemic on respiratory viruses. *Science*, 372(6546):1043–1044, 2021.
- 765 [3] Mihaly Koltai, Fabienne Krauer, David Hodgson, Edwin van Leeuwen, Marina
766 Treskova-Schwarzbach, Mark Jit, and Stefan Flasche. Determinants of RSV
767 epidemiology following suppression through pandemic contact restrictions. *Epi-
768 demics*, 40:100614, 2022.
- 769 [4] Sang Woo Park, Brooklyn Noble, Emily Howerton, Bjarke F Nielsen, Sarah
770 Lentz, Lilliam Ambroggio, Samuel Dominguez, Kevin Messacar, and Bryan T
771 Grenfell. Predicting the impact of non-pharmaceutical interventions against
772 COVID-19 on *Mycoplasma pneumoniae* in the United States. *Epidemics*,
773 49:100808, 2024.
- 774 [5] Amanda C Perofsky, Chelsea L Hansen, Roy Burstein, Shanda Boyle, Robin
775 Prentice, Cooper Marshall, David Reinhart, Ben Capodanno, Melissa Truong,
776 Kristen Schwabe-Fry, et al. Impacts of human mobility on the citywide trans-
777 mission dynamics of 18 respiratory viruses in pre-and post-COVID-19 pandemic
778 years. *Nature communications*, 15(1):4164, 2024.
- 779 [6] Eric J Chow, Timothy M Uyeki, and Helen Y Chu. The effects of the COVID-19
780 pandemic on community respiratory virus activity. *Nature Reviews Microbiol-
781 ogy*, 21(3):195–210, 2023.
- 782 [7] Stephen M Kissler, Christine Tedijanto, Edward Goldstein, Yonatan H Grad,
783 and Marc Lipsitch. Projecting the transmission dynamics of SARS-CoV-2
784 through the postpandemic period. *Science*, 368(6493):860–868, 2020.
- 785 [8] Rachel E Baker, Chadi M Saad-Roy, Sang Woo Park, Jeremy Farrar, C Jessica E
786 Metcalf, and Bryan T Grenfell. Long-term benefits of nonpharmaceutical inter-
787 ventions for endemic infections are shaped by respiratory pathogen dynamics.
788 *Proceedings of the National Academy of Sciences*, 119(49):e2208895119, 2022.
- 789 [9] Maaike C Swets, Clark D Russell, Ewen M Harrison, Annemarie B Docherty,
790 Nazir Lone, Michelle Girvan, Hayley E Hardwick, Leonardus G Visser, Pe-
791 ter JM Openshaw, Geert H Groeneveld, et al. SARS-CoV-2 co-infection with
792 influenza viruses, respiratory syncytial virus, or adenoviruses. *The Lancet*,
793 399(10334):1463–1464, 2022.

- 794 [10] Chun-Yang Lin, Joshua Wolf, David C Brice, Yilun Sun, Macauley Locke,
795 Sean Cherry, Ashley H Castellaw, Marie Wehenkel, Jeremy Chase Crawford,
796 Veronika I Zarnitsyna, et al. Pre-existing humoral immunity to human common
797 cold coronaviruses negatively impacts the protective SARS-CoV-2 antibody re-
798 sponse. *Cell host & microbe*, 30(1):83–96, 2022.
- 799 [11] Sam M Murray, Azim M Ansari, John Frater, Paul Klenerman, Susanna
800 Dunachie, Eleanor Barnes, and Ane Ogbe. The impact of pre-existing cross-
801 reactive immunity on SARS-CoV-2 infection and vaccine responses. *Nature
Reviews Immunology*, 23(5):304–316, 2023.
- 803 [12] John-Sebastian Eden, Chisha Sikazwe, Ruopeng Xie, Yi-Mo Deng, Sheena G
804 Sullivan, Alice Michie, Avram Levy, Elena Cutmore, Christopher C Blyth,
805 Philip N Britton, et al. Off-season RSV epidemics in Australia after easing
806 of COVID-19 restrictions. *Nature communications*, 13(1):2884, 2022.
- 807 [13] Stuart L Pimm. The structure of food webs. *Theoretical population biology*,
808 16(2):144–158, 1979.
- 809 [14] Michael G Neubert and Hal Caswell. Alternatives to resilience for measuring
810 the responses of ecological systems to perturbations. *Ecology*, 78(3):653–665,
811 1997.
- 812 [15] Lance H Gunderson. Ecological resilience—in theory and application. *Annual
813 review of ecology and systematics*, 31(1):425–439, 2000.
- 814 [16] Vasilis Dakos and Sonia Kéfi. Ecological resilience: what to measure and how.
815 *Environmental Research Letters*, 17(4):043003, 2022.
- 816 [17] Floris Takens. Detecting strange attractors in turbulence. In *Dynamical Sys-
817 tems and Turbulence, Warwick 1980: proceedings of a symposium held at the
818 University of Warwick 1979/80*, pages 366–381. Springer, 2006.
- 819 [18] Jonathan Dushoff, Joshua B Plotkin, Simon A Levin, and David JD Earn.
820 Dynamical resonance can account for seasonality of influenza epidemics. *Pro-
821 ceedings of the National Academy of Sciences*, 101(48):16915–16916, 2004.
- 822 [19] Alan Hastings, Karen C Abbott, Kim Cuddington, Tessa Francis, Gabriel Gell-
823 ner, Ying-Cheng Lai, Andrew Morozov, Sergei Petrovskii, Katherine Scran-
824 ton, and Mary Lou Zeeman. Transient phenomena in ecology. *Science*,
825 361(6406):eaat6412, 2018.
- 826 [20] Matthew B Kennel, Reggie Brown, and Henry DI Abarbanel. Determining
827 embedding dimension for phase-space reconstruction using a geometrical con-
828 struction. *Physical review A*, 45(6):3403, 1992.

- 829 [21] Eugene Tan, Shannon Algar, Débora Corrêa, Michael Small, Thomas Stemler,
830 and David Walker. Selecting embedding delays: An overview of embedding
831 techniques and a new method using persistent homology. *Chaos: An Interdis-*
832 *ciplinary Journal of Nonlinear Science*, 33(3), 2023.
- 833 [22] Bjarke Frost Nielsen, Sang Woo Park, Emily Howerton, Olivia Frost Lorentzen,
834 Mogens H Jensen, and Bryan T Grenfell. Complex multiannual cycles of My-
835 coplasma pneumoniae: persistence and the role of stochasticity. *arXiv*, 2025.
- 836 [23] Jennifer M Radin, Anthony W Hawksworth, Peter E Kammerer, Melinda Bal-
837 ansay, Rema Raman, Suzanne P Lindsay, and Gary T Brice. Epidemiology
838 of pathogen-specific respiratory infections among three US populations. *PLoS*
839 *One*, 9(12):e114871, 2014.
- 840 [24] Guojian Lv, Limei Shi, Yi Liu, Xuecheng Sun, and Kai Mu. Epidemiological
841 characteristics of common respiratory pathogens in children. *Scientific Reports*,
842 14(1):16299, 2024.
- 843 [25] Saverio Caini, Adam Meijer, Marta C Nunes, Laetitia Henaff, Malaika Zounon,
844 Bronke Boudewijns, Marco Del Riccio, and John Paget. Probable extinction of
845 influenza b/yamagata and its public health implications: a systematic literature
846 review and assessment of global surveillance databases. *The Lancet Microbe*,
847 2024.
- 848 [26] Zhiyuan Chen, Joseph L-H Tsui, Bernardo Gutierrez, Simon Busch Moreno,
849 Louis du Plessis, Xiaowei Deng, Jun Cai, Sumali Bajaj, Marc A Suchard,
850 Oliver G Pybus, et al. COVID-19 pandemic interventions reshaped the global
851 dispersal of seasonal influenza viruses. *Science*, 386(6722):eadq3003, 2024.
- 852 [27] Bryan T Grenfell, Ottar N Bjørnstad, and Bärbel F Finkenstädt. Dynamics of
853 measles epidemics: scaling noise, determinism, and predictability with the TSIR
854 model. *Ecological monographs*, 72(2):185–202, 2002.
- 855 [28] Samit Bhattacharyya, Per H Gesteland, Kent Korgenski, Ottar N Bjørnstad,
856 and Frederick R Adler. Cross-immunity between strains explains the dynamical
857 pattern of paramyxoviruses. *Proceedings of the National Academy of Sciences*,
858 112(43):13396–13400, 2015.
- 859 [29] Virginia E Pitzer, Cécile Viboud, Wladimir J Alonso, Tanya Wilcox, C Jessica
860 Metcalf, Claudia A Steiner, Amber K Haynes, and Bryan T Grenfell. Environ-
861 mental drivers of the spatiotemporal dynamics of respiratory syncytial virus in
862 the United States. *PLoS pathogens*, 11(1):e1004591, 2015.
- 863 [30] Katharine R Dean, Fabienne Krauer, Lars Walløe, Ole Christian Lingjærde, Bar-
864 bara Bramanti, Nils Chr Stenseth, and Boris V Schmid. Human ectoparasites
865 and the spread of plague in Europe during the Second Pandemic. *Proceedings*
866 *of the National Academy of Sciences*, 115(6):1304–1309, 2018.

- 867 [31] Margarita Pons-Salort and Nicholas C Grassly. Serotype-specific immunity
868 explains the incidence of diseases caused by human enteroviruses. *Science*,
869 361(6404):800–803, 2018.
- 870 [32] Sarah Cobey and Edward B Baskerville. Limits to causal inference with state-
871 space reconstruction for infectious disease. *PLoS one*, 11(12):e0169050, 2016.
- 872 [33] Public Health Agency of Canada. Respiratory virus detections in
873 Canada. 2024. <https://www.canada.ca/en/public-health/services/surveillance/respiratory-virus-detections-canada.html>. Accessed Sep
874 4, 2024.
- 876 [34] Centre for Health Protection. Detection of pathogens from respiratory spec-
877 imens. 2024. <https://www.chp.gov.hk/en/statistics/data/10/641/642/2274.html>. Accessed Nov 20, 2024.
- 879 [35] Centre for Health Protection. Detection of gastroenteritis viruses from faecal
880 specimens. 2024. <https://www.chp.gov.hk/en/statistics/data/10/641/717/3957.html>. Accessed Nov 20, 2024.
- 882 [36] Korea Disease Control and Prevention Agency. Acute respiratory infection,
883 Sentinel surveillance infectious diseases. 2024. <https://dportal.kdca.go.kr/pot/is/st/ari.do>. Accessed Nov 20, 2024.
- 885 [37] Edward Goldstein, Sarah Cobey, Saki Takahashi, Joel C Miller, and Marc Lipsitch.
886 Predicting the epidemic sizes of influenza A/H1N1, A/H3N2, and B: a
887 statistical method. *PLoS medicine*, 8(7):e1001051, 2011.
- 888 [38] Sang Woo Park, Inga Holmdahl, Emily Howerton, Wenchang Yang, Rachel E
889 Baker, Gabriel A Vecchi, Sarah Cobey, C Jessica E Metcalf, and Bryan T Gren-
890 fell. Interplay between climate, childhood mixing, and population-level suscep-
891 tibility explains a sudden shift in RSV seasonality in Japan. *medRxiv*, pages
892 2025–03, 2025.
- 893 [39] Bob Carpenter, Andrew Gelman, Matthew D Hoffman, Daniel Lee, Ben
894 Goodrich, Michael Betancourt, Marcus A Brubaker, Jiqiang Guo, Peter Li,
895 and Allen Riddell. Stan: A probabilistic programming language. *Journal of
896 statistical software*, 76, 2017.
- 897 [40] Stan Development Team. RStan: the R interface to Stan, 2024. R package
898 version 2.32.6.

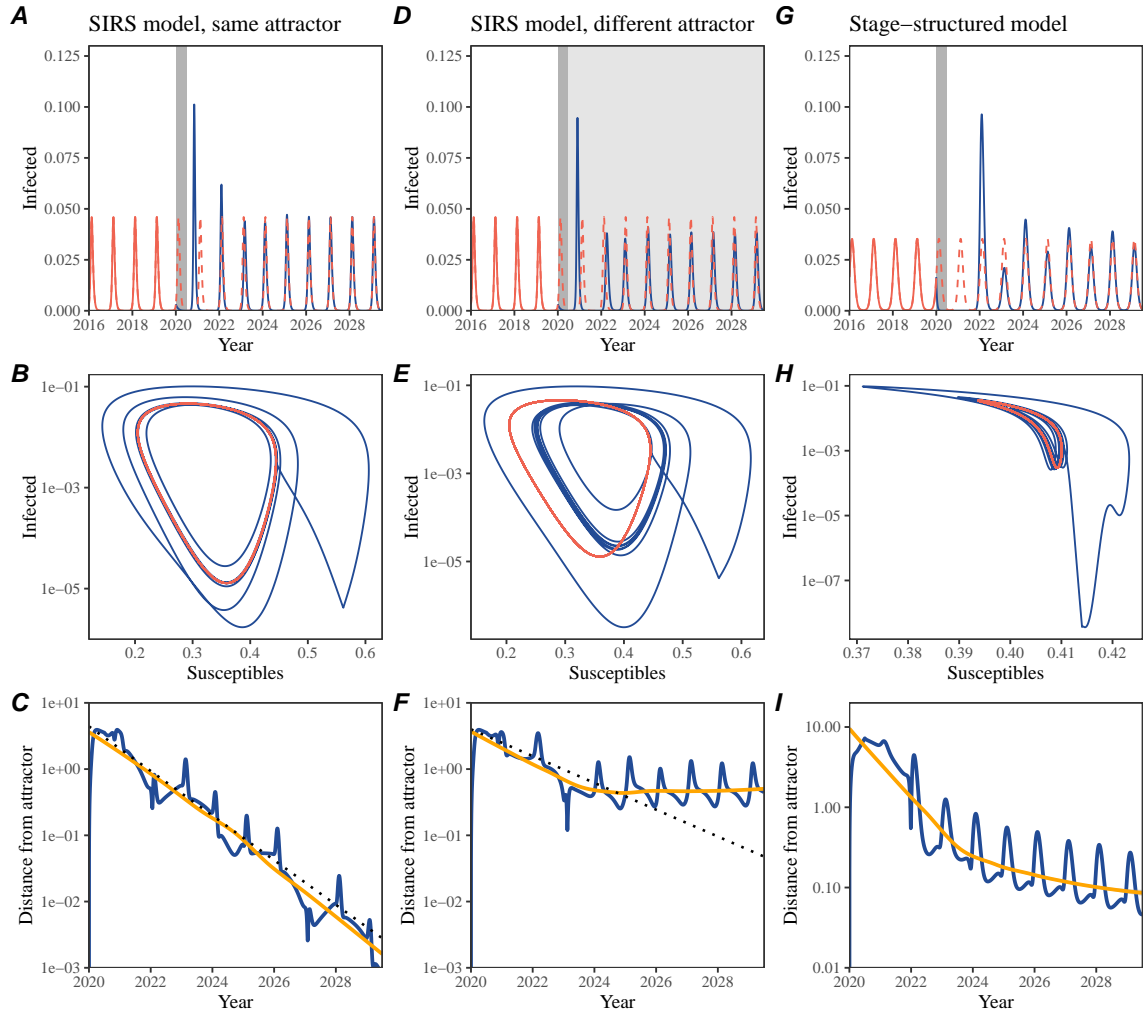


Figure 2: A simple method to measure pathogen resilience following pandemic perturbations across different scenarios. (A, D, G) Simulated epidemic trajectories across various models. Red and blue solid lines represent epidemic dynamics before and after pandemic perturbations are introduced, respectively. Red dashed lines represent counterfactual epidemic dynamics in the absence of perturbations. Gray regions indicate the duration of perturbations with the dark gray region representing a 50% transmission reduction and the light gray region representing a 10% transmission reduction. (B, E, H) Phase plane representation of the time series in panels A, D, and G alongside the corresponding susceptible host dynamics. Red and blue solid lines represent epidemic trajectories on an SI phase plane before and after perturbations are introduced, respectively. (C, F, I) Changes in distance from the attractor over time on a log scale. Blue lines represent the distance from the attractor. Orange lines represent the locally estimated scatterplot smoothing (LOESS) fits to the logged distance from the attractor. Dotted lines show the intrinsic resilience of the seasonally unforced system.

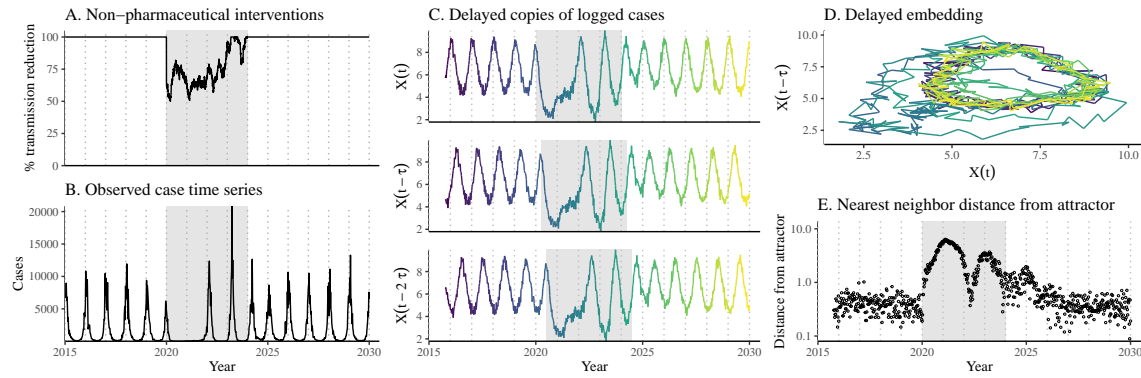


Figure 3: A schematic diagram explaining the inference of pathogen resilience from synthetic data. (A) A realistic example of simulated pandemic perturbations, represented by a relative reduction in transmission. (B) The impact of the synthetic pandemic perturbation on epidemic dynamics simulated using a SIRS model with demographic stochasticity. (C) Generating delayed copies of the logged time series allows us to obtain an embedding. (D) Two dimensional representation of an embedding. (E) Delayed embedding allows us to calculate the nearest neighbor distance from the empirical attractor, which is determined based on the pre-pandemic time series. This distance time series can be used to infer pathogen resilience after choosing an appropriate window for linear regression.

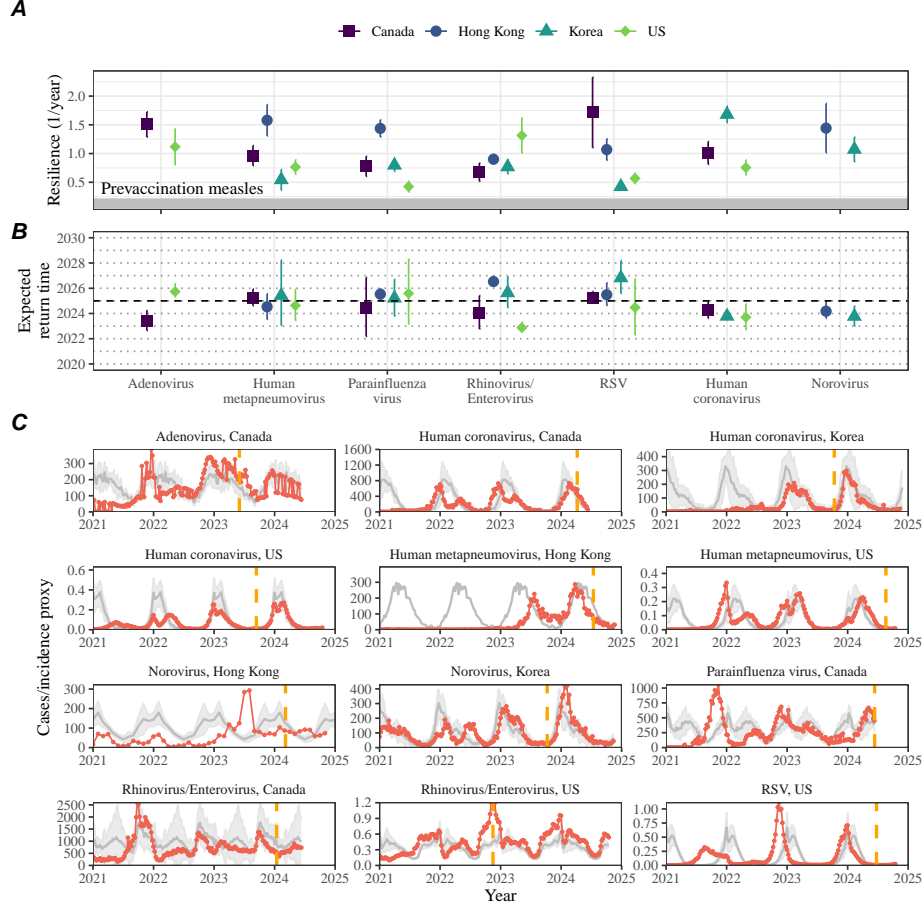


Figure 4: **Summary of resilience estimates and predictions for return time.** (A) Estimated pathogen resilience. The gray horizontal line represents the intrinsic resilience of pre-vaccination measles dynamics. (B) Predicted timing of when each pathogen will return to their pre-pandemic cycles. The dashed line in panel B indicates the end of 2024. Error bars represent 95% confidence intervals. (C) Observed dynamics for pathogen that are predicted to have returned before the end of 2024. Red points and lines represent data before 2020. Gray lines and shaded regions represent the mean seasonal patterns and corresponding 95% confidence intervals around the mean, previously shown in Figure 1. Orange vertical lines represent the predicted timing of return.

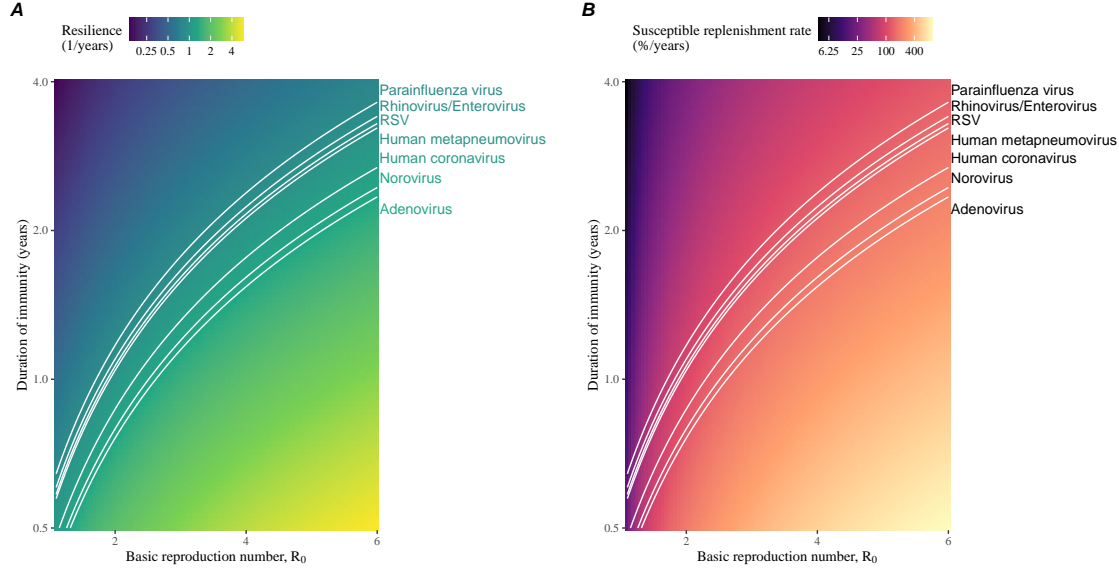


Figure 5: Linking pathogen resilience to epidemiological parameters and susceptible host dynamics. (A) Intrinsic resilience as a function of the basic reproduction number \mathcal{R}_0 and the duration of immunity. (B) Per-capita susceptible replenishment rate as a function of the basic reproduction number \mathcal{R}_0 and the duration of immunity. The standard SIRS model without seasonal forcing is used to compute intrinsic resilience and the per-capita susceptible replenishment rate. Lines correspond to a set of parameters that are consistent with mean resilience estimates for each pathogen, averaged across different countries.

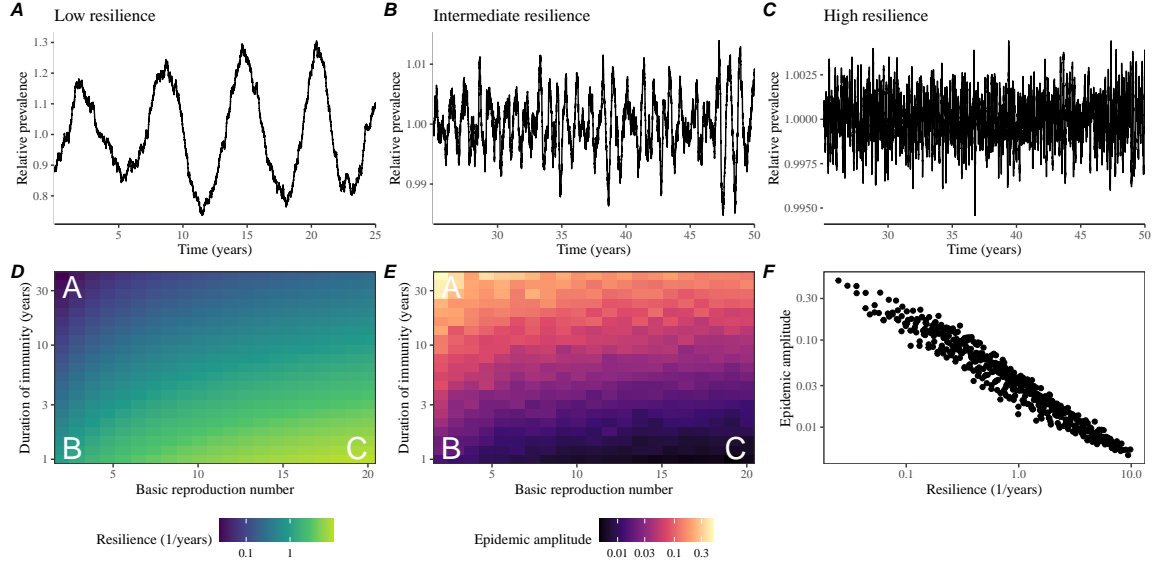


Figure 6: Linking resilience of a host-pathogen system to its sensitivity to stochastic perturbations. (A–C) Epidemic trajectories of a stochastic SIRS model across three different resilience values: low, intermediate, and high. The relative prevalence was calculated by dividing infection prevalence by its mean value. (D) Intrinsic resilience of a system as a function of the basic reproduction number \mathcal{R}_0 and the duration of immunity. (E) Epidemic amplitude as a function of the basic reproduction number \mathcal{R}_0 and the duration of immunity. The epidemic amplitude corresponds to $(\max I - \min I)/(2\bar{I})$, where \bar{I} represents the mean prevalence. Labels A–C in panels D and E correspond to scenarios shown in panels A–C. (F) The relationship between pathogen resilience and epidemic amplitude.

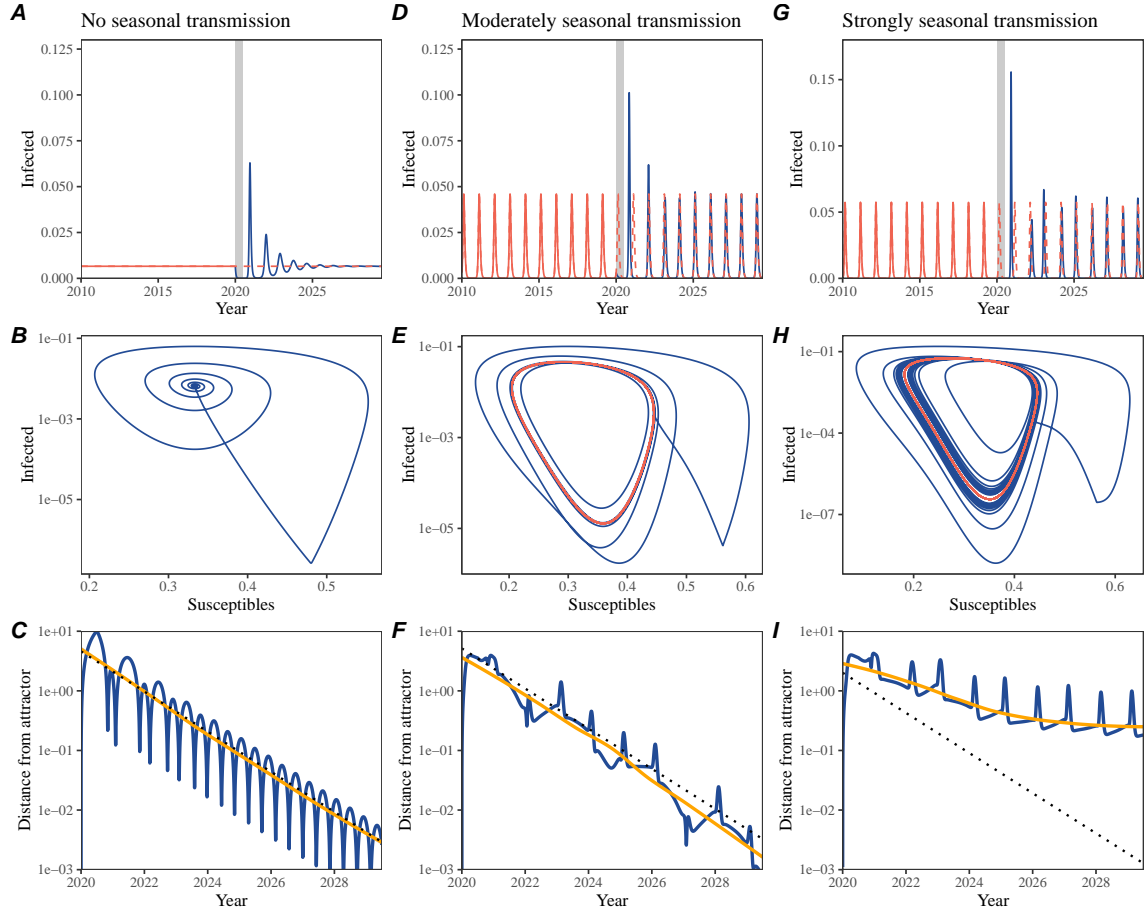


Figure S1: Impact of seasonal transmission on pathogen resilience. (A, D, G) Simulated epidemic trajectories using the SIRS model without seasonal forcing (A), with seasonal forcing of amplitude of 0.2 (D), and with seasonal forcing of amplitude of 0.4 (G). Red and blue solid lines represent epidemic dynamics before and after interventions are introduced, respectively. Red dashed lines represent counterfactual epidemic dynamics in the absence of interventions. Gray regions indicate the duration of interventions. (B, E, H) Phase plane representation of the time series in panels A, D, and G alongside the corresponding susceptible host dynamics. Red and blue solid lines represent epidemic trajectories on an SI phase plane before and after interventions are introduced, respectively. (C, F, I) Changes in logged distance from the attractor over time. Blue lines represent the logged distance from the attractor. Orange lines represent the locally estimated scatterplot smoothing (LOESS) fits to the logged distance from the attractor. Dotted lines show the intrinsic resilience of the seasonally unforced system.

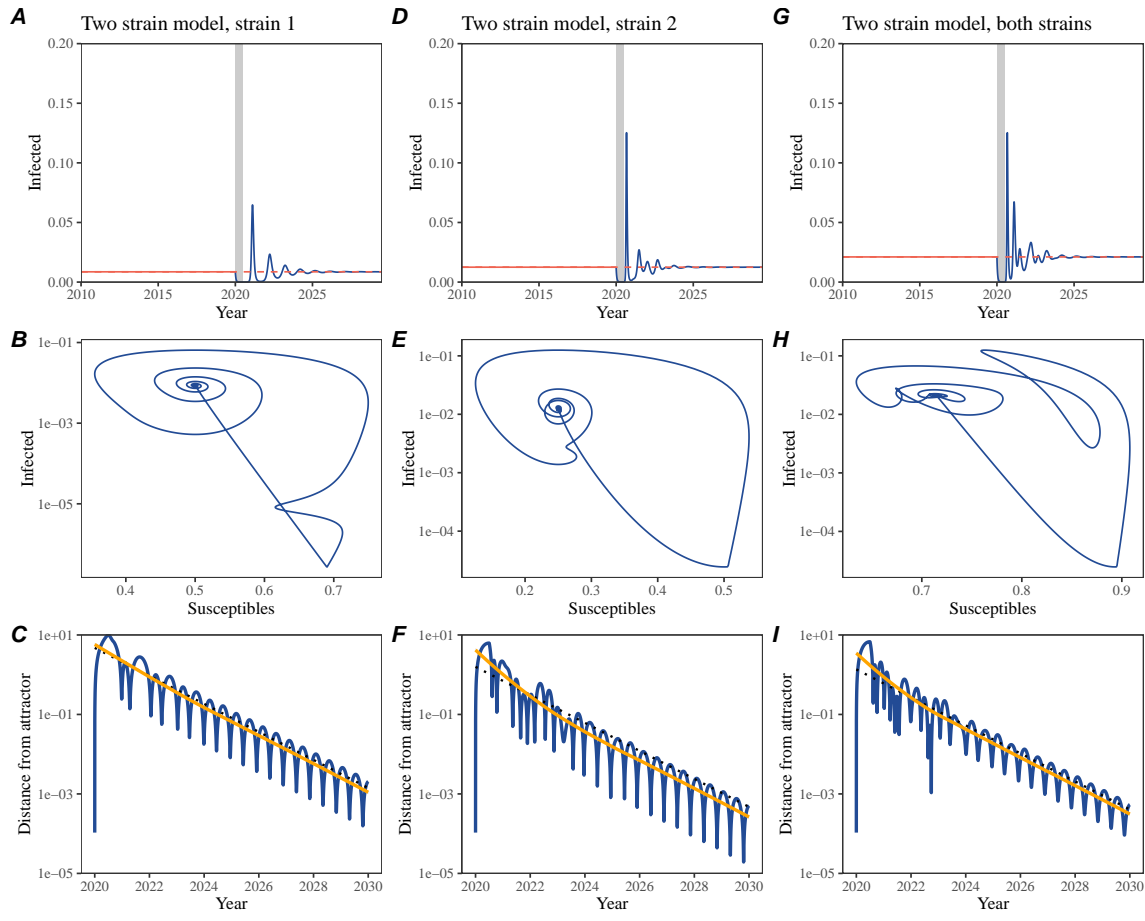


Figure S2: A simple method to measure pathogen resilience following pandemic perturbations for a two-strain competition system without seasonal forcing. (A, D, G) Simulated epidemic trajectories using a two-strain system without seasonal forcing. In this model, two strains compete through cross immunity. Red and blue solid lines represent epidemic dynamics before and after interventions are introduced, respectively. Red dashed lines represent counterfactual epidemic dynamics in the absence of interventions. Gray regions indicate the duration of interventions. (B, E, H) Phase plane representation of the time series in panels A, D, and G alongside the corresponding susceptible host dynamics. Blue solid lines represent epidemic trajectories on an SI phase plane before and after interventions are introduced, respectively. (C, F, I) Changes in logged distance from the attractor over time. Blue lines represent the logged distance from the attractor. Orange lines represent the locally estimated scatterplot smoothing (LOESS) fits to the logged distance from the attractor. Dotted lines show the intrinsic resilience of the seasonally unforced system.

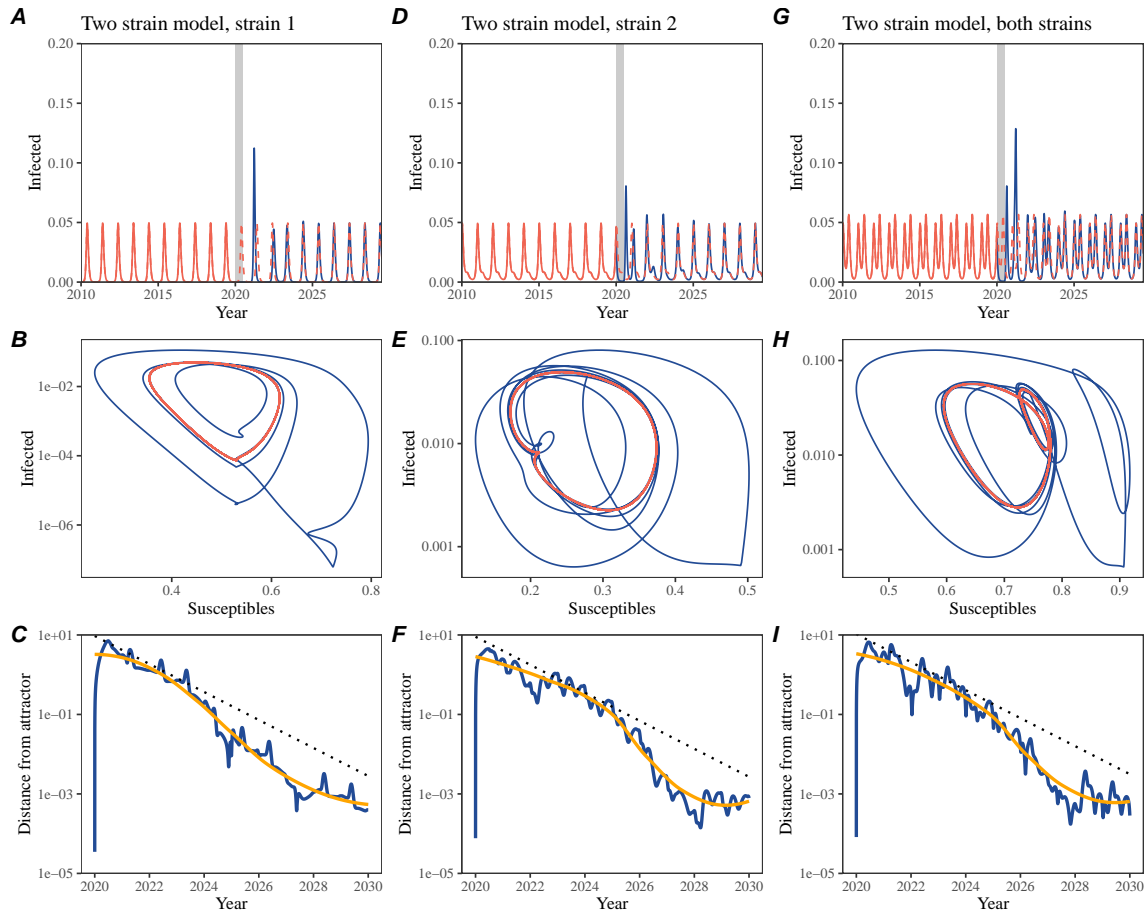


Figure S3: A simple method to measure pathogen resilience following pandemic perturbations for a two-strain competition system with seasonal forcing. (A, D, G) Simulated epidemic trajectories using a two-strain system with seasonal forcing (amplitude of 0.2). In this model, two strains compete through cross immunity. Red and blue solid lines represent epidemic dynamics before and after interventions are introduced, respectively. Red dashed lines represent counterfactual epidemic dynamics in the absence of interventions. Gray regions indicate the duration of interventions. (B, E, H) Phase plane representation of the time series in panels A, D, and G alongside the corresponding susceptible host dynamics. Red and blue solid lines represent epidemic trajectories on an SI phase plane before and after interventions are introduced, respectively. (C, F, I) Changes in logged distance over time. Blue lines represent the logged distance from the attractor. Orange lines represent the locally estimated scatterplot smoothing (LOESS) fits to the logged distance from the attractor. Dotted lines show the intrinsic resilience of the seasonally unforced system.

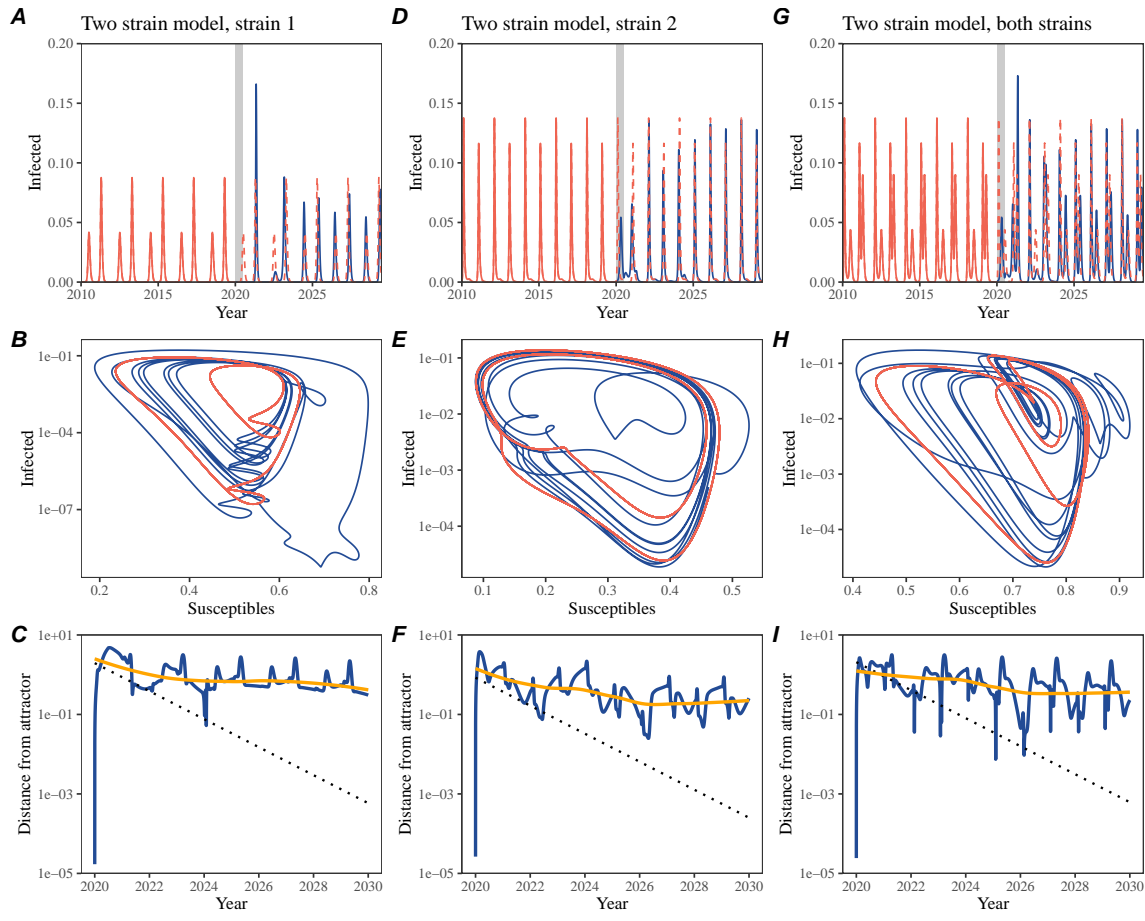


Figure S4: A simple method to measure pathogen resilience following pandemic perturbations for a multi-strain competition system with strong seasonal forcing. (A, D, G) Simulated epidemic trajectories using a two-strain system with seasonal forcing (amplitude of 0.2). In this model, two strains compete through cross immunity. Red and blue solid lines represent epidemic dynamics before and after interventions are introduced, respectively. Red dashed lines represent counterfactual epidemic dynamics in the absence of interventions. Gray regions indicate the duration of interventions. (B, E, H) Phase plane representation of the time series in panels A, D, and G alongside the corresponding susceptible host dynamics. Red and blue solid lines represent epidemic trajectories on an SI phase plane before and after interventions are introduced, respectively. (C, F, I) Changes in logged distance over time. Blue lines represent the logged distance from the attractor. Orange lines represent the locally estimated scatterplot smoothing (LOESS) fits to the logged distance from the attractor. Dotted lines show the intrinsic resilience of the seasonally unforced system.

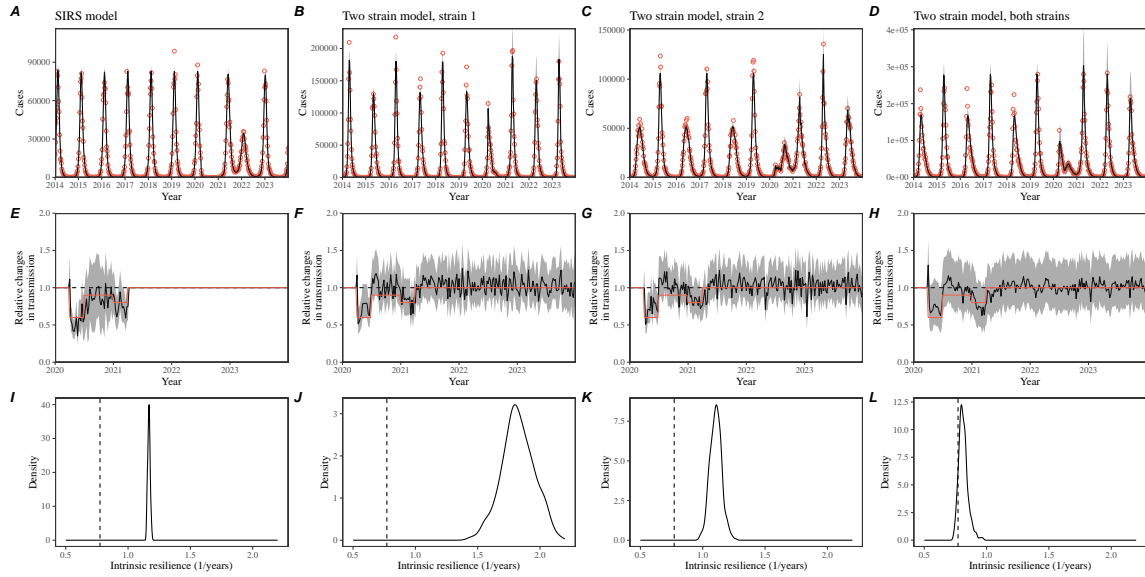


Figure S5: Mechanistic model fits to simulated data and inferred intrinsic resilience. We simulated discrete time, stochastic epidemic trajectories using a seasonally forced SIRS model (A,E,I) and a seasonally forced two-strain model (B–D, F–H, and J–L) and tested whether we can estimate the intrinsic resilience of the seasonally unforced versions of the model by fitting a mechanistic model (Supplementary Text). We fitted the same discrete time, one strain, deterministic SIRS model in each scenario. (A–D) Simulated case time series from corresponding models shown in the title (red) and SIRS model fits (black). (E–H) Assumed changes in transmission due to pandemic perturbations (red) and estimated time-varying relative transmission rates for the perturbation impact from the SIRS model fits (black). Solid lines and shaded regions represent fitted posterior median and 95% credible intervals. (I–L) Comparisons between the true and estimated intrinsic resilience of the seasonally unforced system. Vertical lines represent the true intrinsic resilience of the seasonally unforced system. Density plots represent the posterior distribution of the inferred intrinsic resilience of the seasonally unforced SIRS model using fitted parameters.

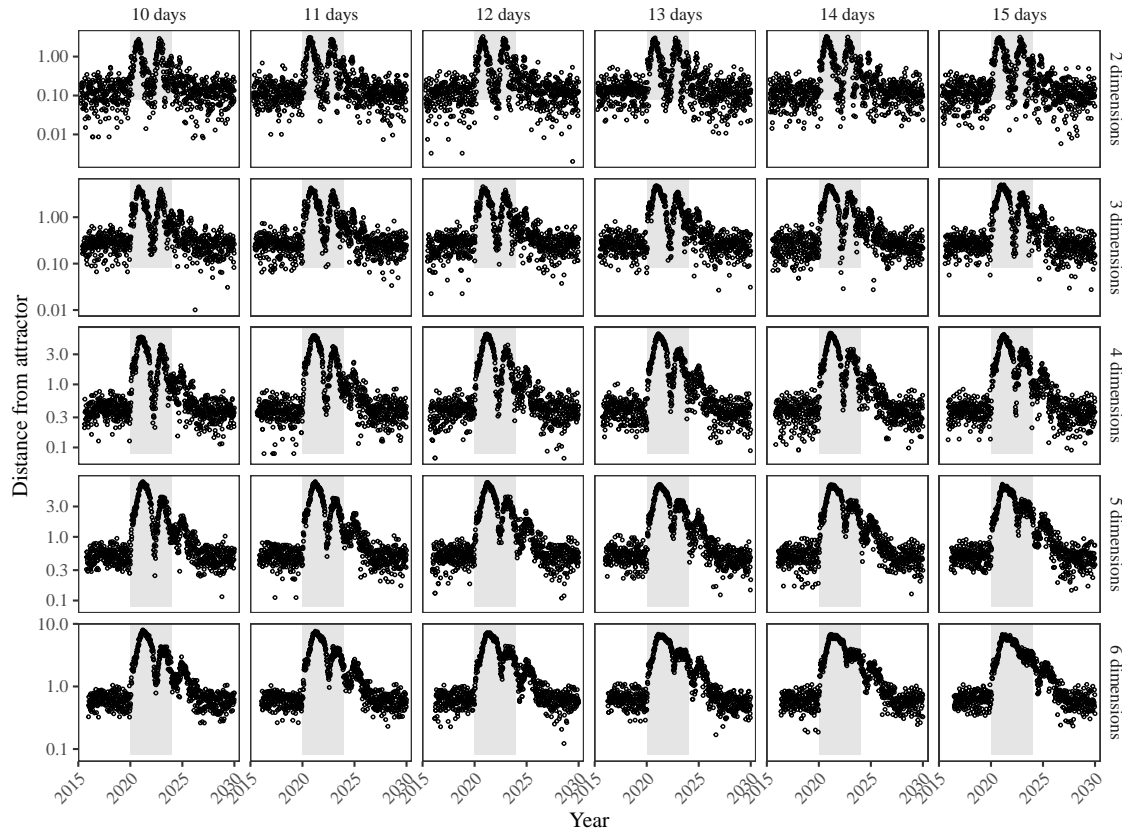


Figure S6: Sensitivity of the distance from the attractor to choice of embedding lags and dimensions. Sensitivity analysis for the distance-from-attractor time series shown in Figure 3E in the main text by varying the embedding lag between 10–15 days and embedding dimensions between 2–6 dimensions. The gray region represents the assumed period of pandemic perturbation.

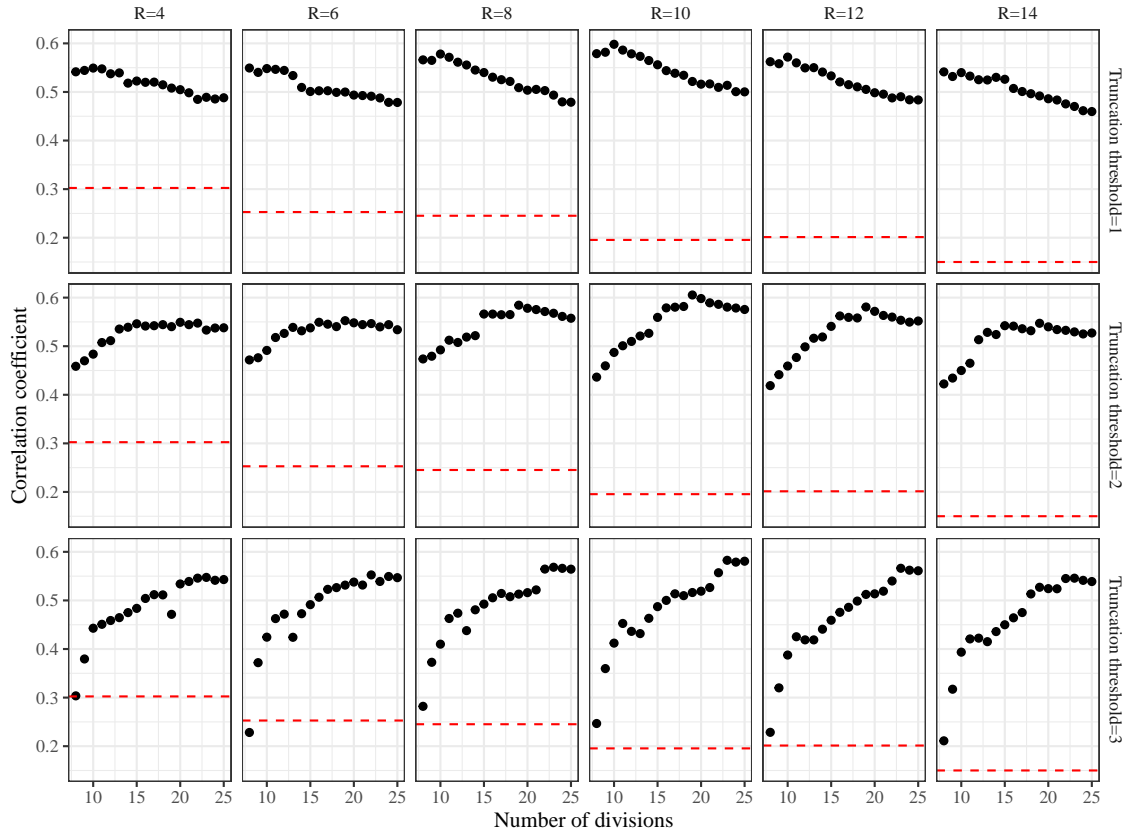


Figure S7: Impact of fitting window selection on the estimation of empirical resilience. We simulated 500 epidemics of a stochastic SIRS model with randomly drawn parameters and randomly generated pandemic perturbations (Supplementary Text). For each simulation, we varied the false nearest neighbor threshold R for reconstructing the empirical attractor as well as the parameters for regression window selection (i.e., the truncation threshold a and the number of divisions K). Each point represents the resulting correlation coefficient between empirical and intrinsic resilience estimates for a given scenario. Dashed lines represent the correlation coefficient between empirical and intrinsic resilience estimates for the naive approach that fits a linear regression on a log scale, starting from the maximum distance until the end of the time series.

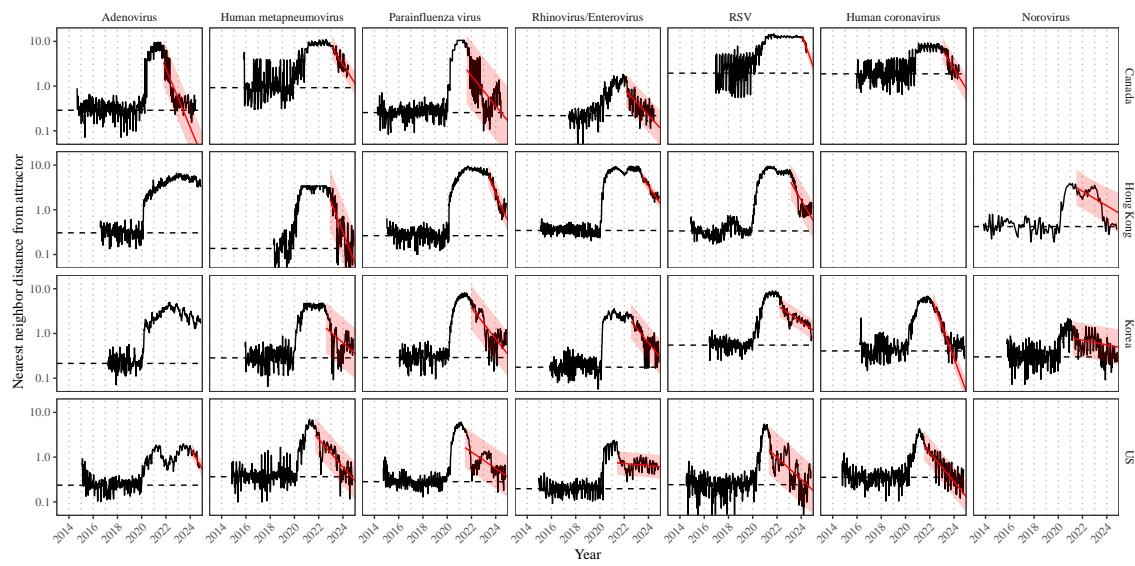


Figure S8: Estimated time series of distance from the attractor for each pathogen and corresponding linear regression fits using automated window selection criterion across Canada, Hong Kong, Korea, and the US. Black lines represent the estimated distance from the attractor. Red lines and shaded regions represent the linear regression fits and corresponding 95% confidence intervals. Dashed lines represent the average of the pre-pandemic nearest neighbor distances.

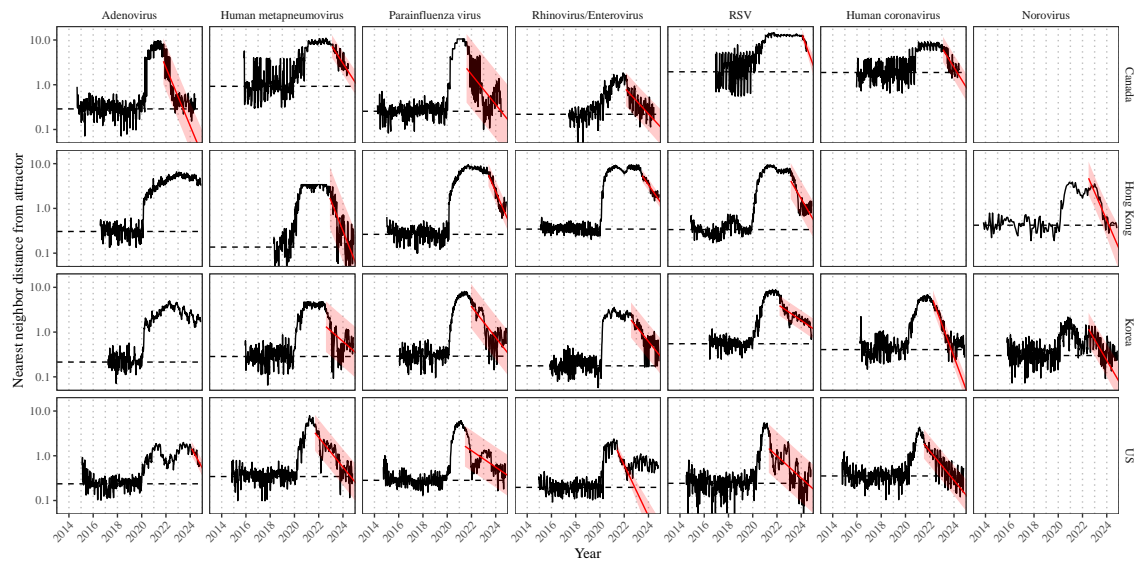


Figure S9: Estimated time series of distance from the attractor for each pathogen and corresponding linear regression fits across Canada, Hong Kong, Korea, and the US, including ad-hoc regression window selection. We used ad-hoc regression windows for norovirus in Hong Kong and Korea and rhinovirus/enterovirus in the US. Black lines represent the estimated distance from the attractor. Red lines and shaded regions represent the linear regression fits and corresponding 95% confidence intervals. Dashed lines represent the average of the pre-pandemic nearest neighbor distances.

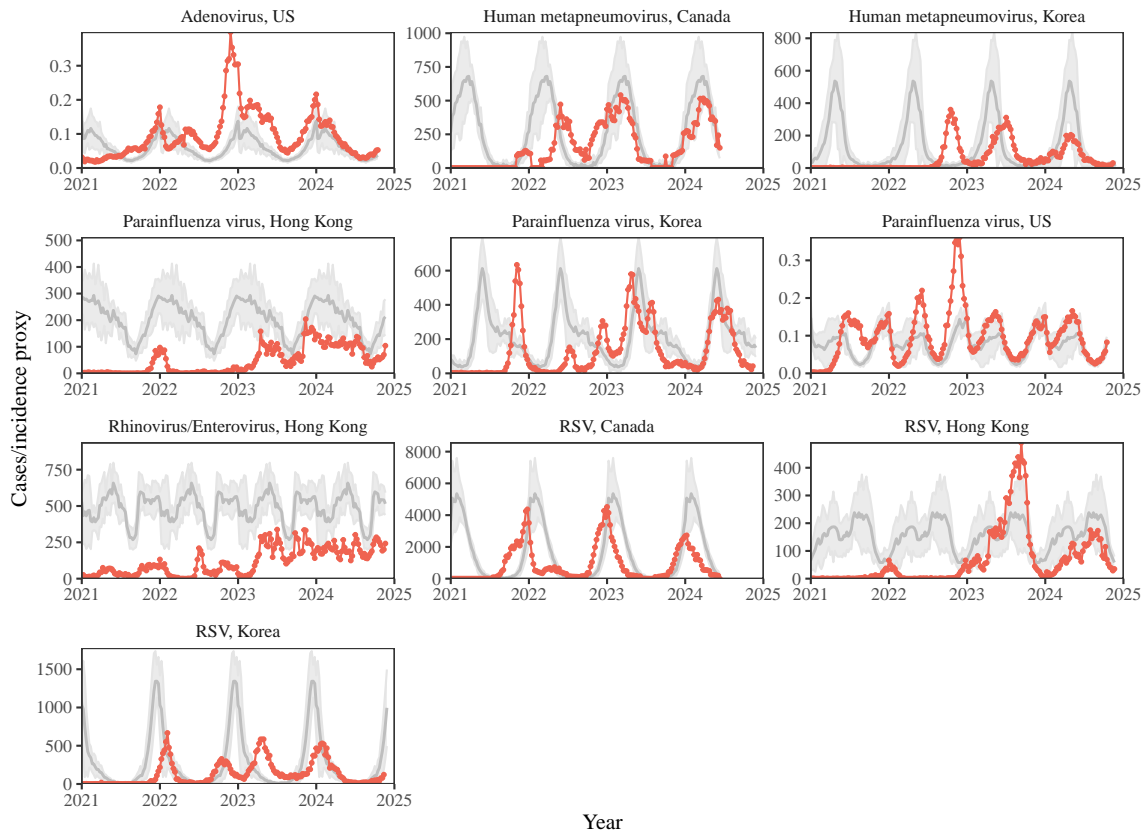


Figure S10: Observed dynamics for pathogen that are predicted to return after the end of 2024. Red points and lines represent data before 2020. Gray lines and shaded regions represent the mean seasonal patterns and corresponding 95% confidence intervals around the mean, previously shown in Figure 1.

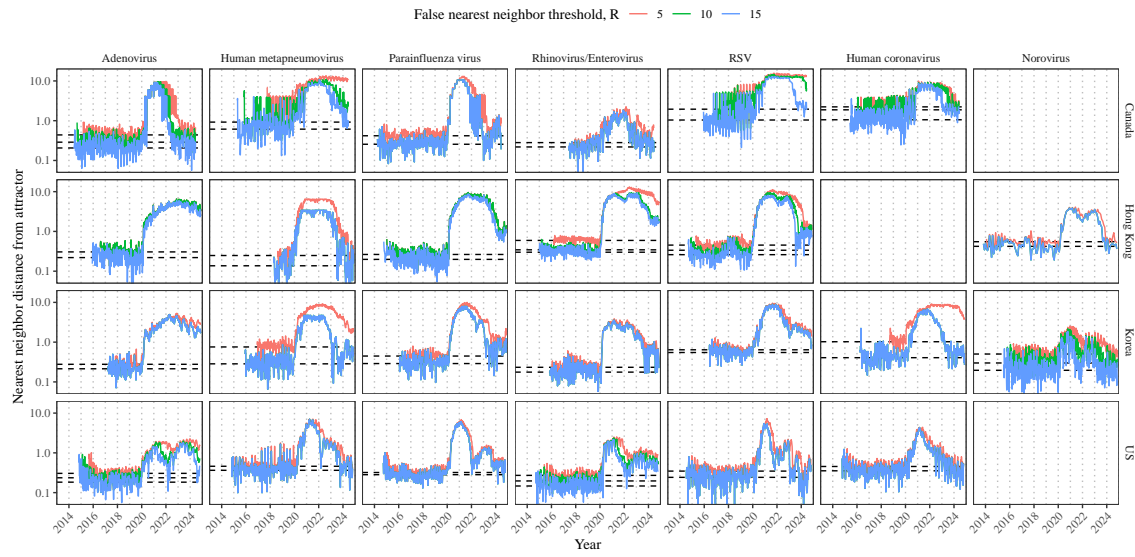


Figure S11: Estimated time series of distance from the attractor for each pathogen across different choices about false nearest neighbor threshold values. Using higher threshold values for the false nearest neighbor approach gives lower embedding dimensions. Colored lines represent the estimated distance from the attractor for different threshold values.

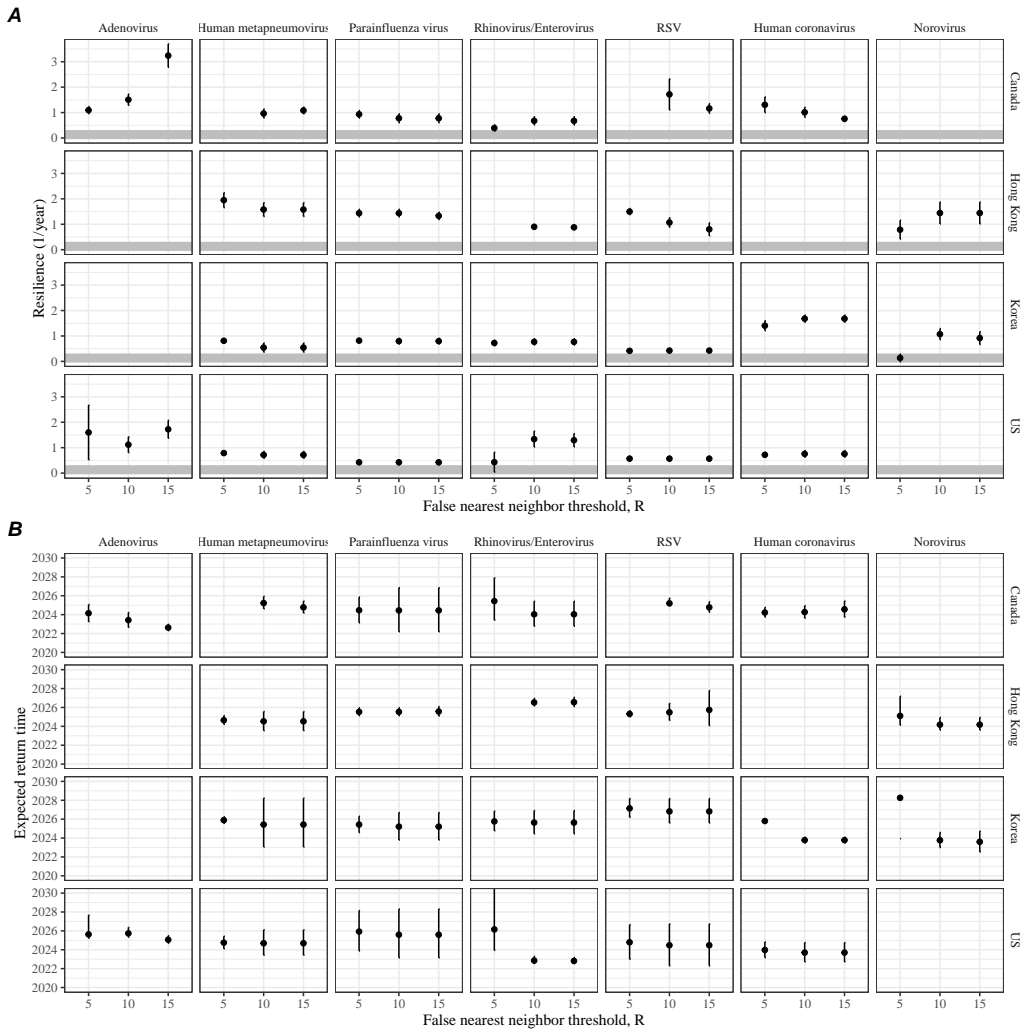


Figure S12: Summary of resilience estimates and predictions for return time across different choices about false nearest neighbor threshold values. The automated window selection method was used for all scenarios to estimate pathogen resilience, except for norovirus in Hong Kong and Korea and rhinovirus/enterovirus in the US. We used the same ad-hoc regression windows for norovirus in Hong Kong and Korea and rhinovirus/enterovirus in the US as we did in the main analysis. (A) Estimated pathogen resilience. The gray horizontal line represents the intrinsic resilience of pre-vaccination measles dynamics. (B) Predicted timing of when each pathogen will return to their pre-pandemic cycles. The dashed line in panel B indicates the end of 2024. Error bars represent 95% confidence intervals.

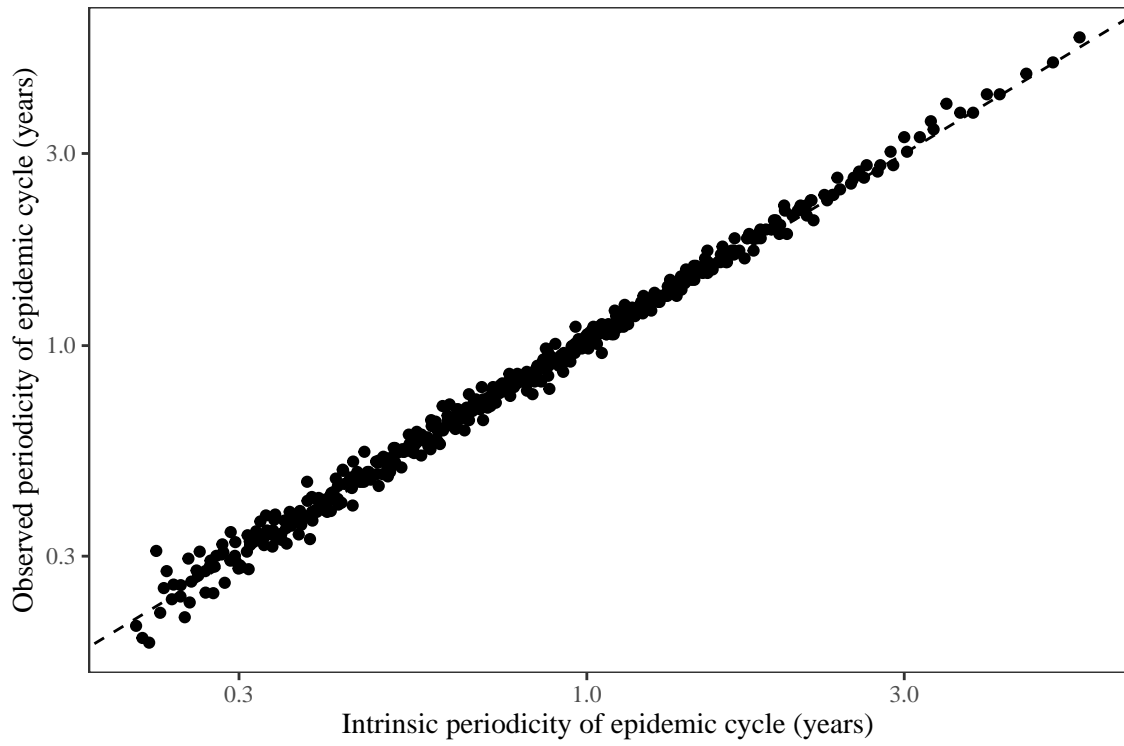


Figure S13: **Comparison between the observed and intrinsic periodicity of the epidemic cycle of the seasonally unforced SIRS model.** The observed periodicity of the epidemic corresponds to the periodicity at which maximum spectral density occurs. The intrinsic periodicity of the epidemic corresponds to $2\pi/\text{Im}(\lambda)$, where $\text{Im}(\lambda)$ is the imaginary part of the eigenvalue.

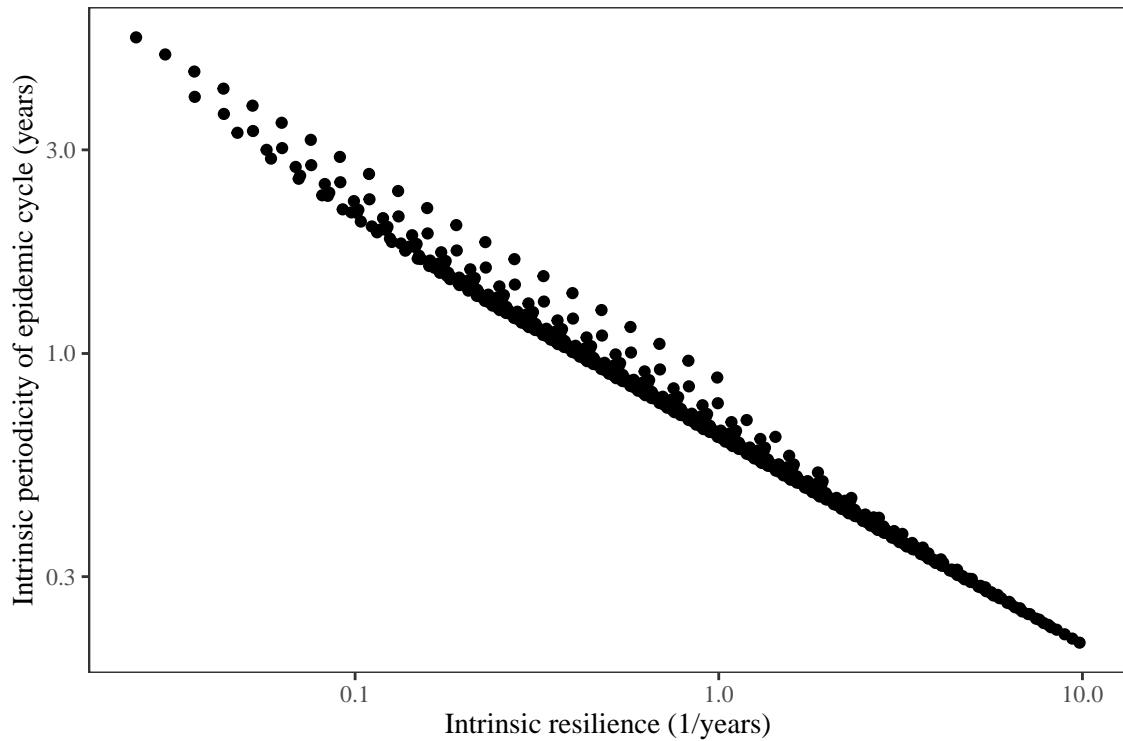


Figure S14: Comparison between the intrinsic resilience and periodicity of the epidemic cycle of the seasonally unforced SIRS model. The intrinsic resilience of the epidemic corresponds to the negative of the real value of the eigenvalue $-\text{Re}(\lambda)$. The intrinsic periodicity of the epidemic corresponds to $2\pi/\text{Im}(\lambda)$, where $\text{Im}(\lambda)$ is the imaginary part of the eigenvalue.

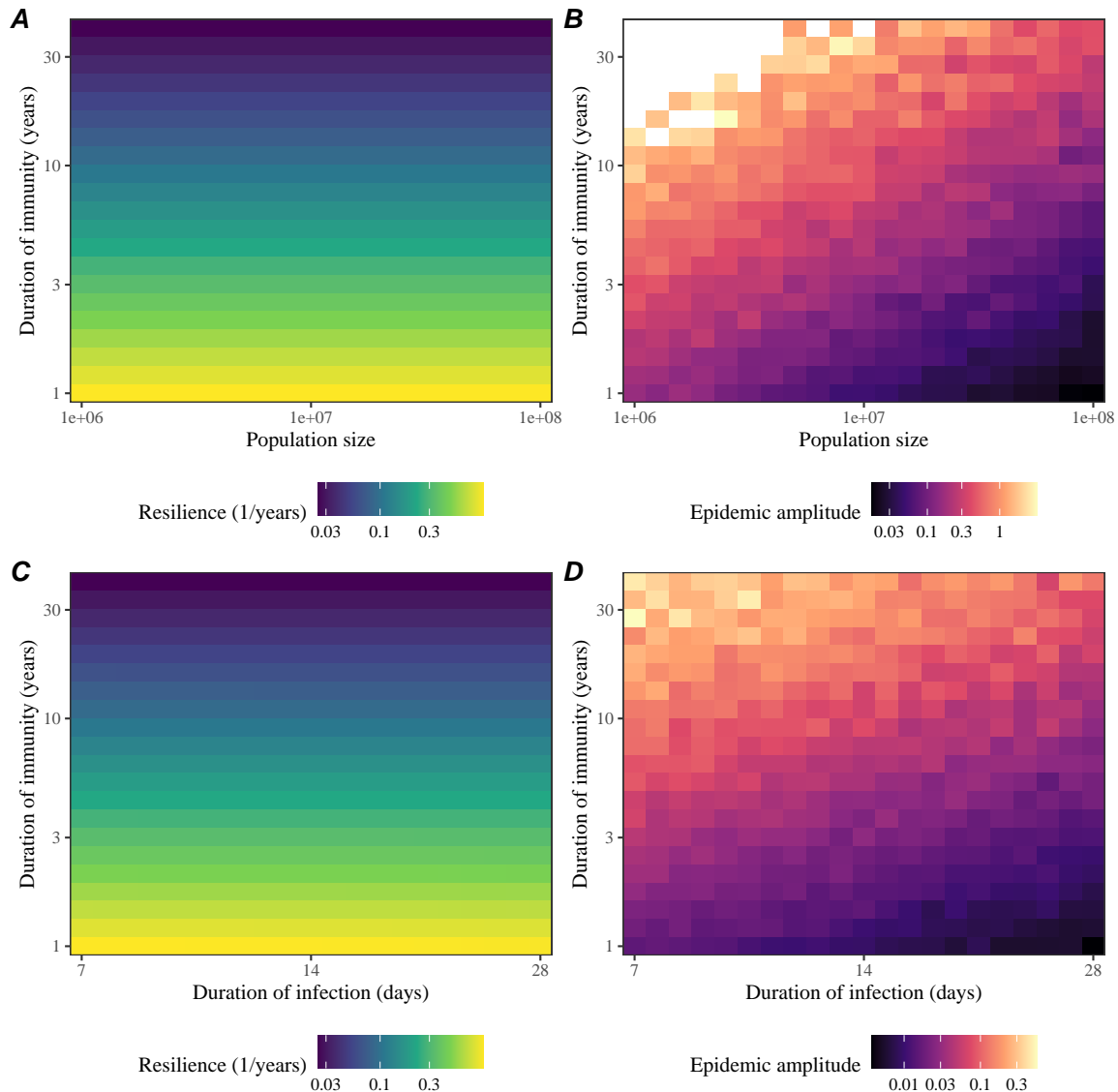


Figure S15: Impact of population size and the average duration of infection of a host-pathogen system to its sensitivity to stochastic perturbations. (A) Intrinsic resilience of a system as a function of population size and the average duration of immunity. (B) Epidemic amplitude as a function of population size and the average duration of immunity. (C) Intrinsic resilience of a system as a function of the average duration of infection and the average duration of immunity. (D) Epidemic amplitude as a function of the average duration of infection and the average duration of immunity. The epidemic amplitude corresponds to $(\max I - \min I)/(2\bar{I})$, where \bar{I} represents the mean prevalence.

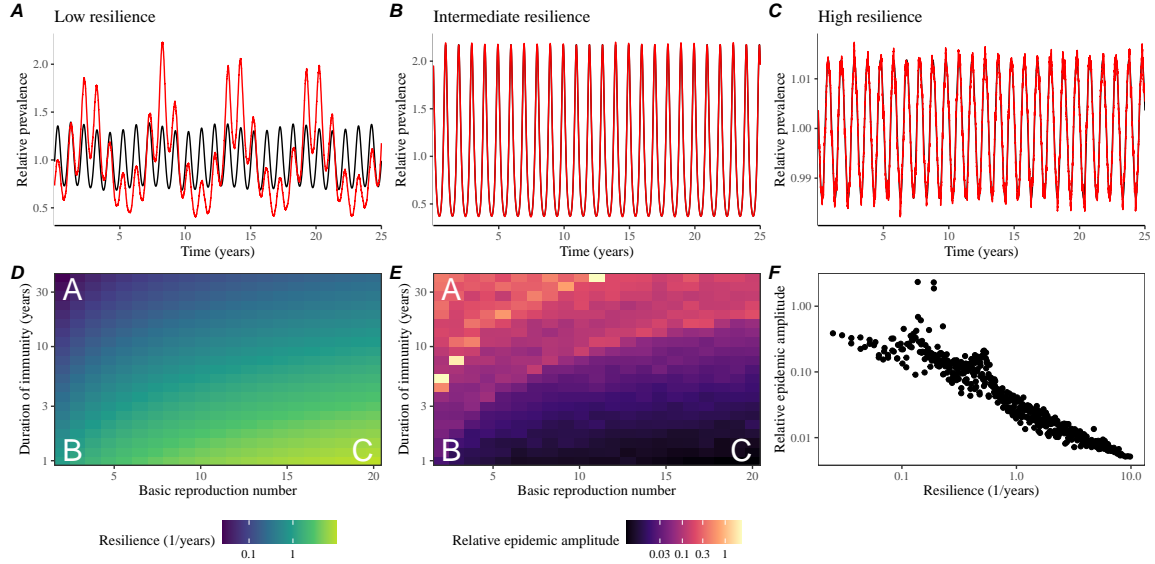


Figure S16: Linking resilience of a host-pathogen system to its sensitivity to stochastic perturbations for the seasonally forced SIRS model. (A–C) Epidemic trajectories of a stochastic SIRS model with demographic stochasticity across three different resilience values: low, intermediate, and high. The relative prevalence was calculated by dividing infection prevalence by its mean value. Black lines represent deterministic epidemic trajectories. Red lines represent stochastic epidemic trajectories. (D) The intrinsic resilience of the seasonally unforced system as a function of the basic reproduction number \mathcal{R}_0 and the duration of immunity. (E) The relative epidemic amplitude, a measure of sensitivity to stochastic perturbations, as a function of the basic reproduction number \mathcal{R}_0 and the duration of immunity. To calculate the relative epidemic amplitude, we first take the relative difference in infection prevalence between stochastic and deterministic trajectories: $\epsilon = (I_{\text{stoch}} - I_{\text{det}})/I_{\text{det}}$. Then, we calculate the difference between maximum and minimum of the relative difference and divide by half: $(\max \epsilon - \min \epsilon)/2$. Labels A–C in panels D and E correspond to scenarios shown in panels A–C. (F) The relationship between pathogen resilience and relative epidemic amplitude.

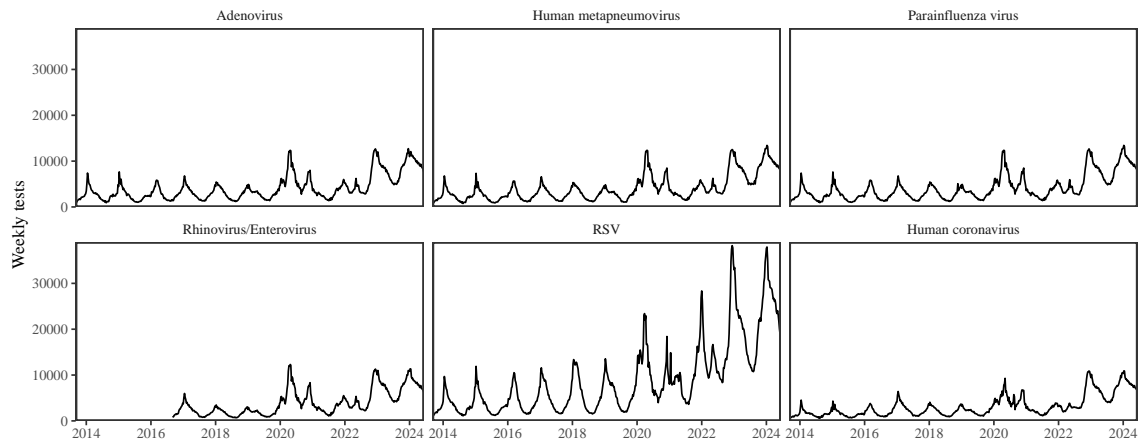


Figure S17: Testing patterns for respiratory pathogens in Canada.

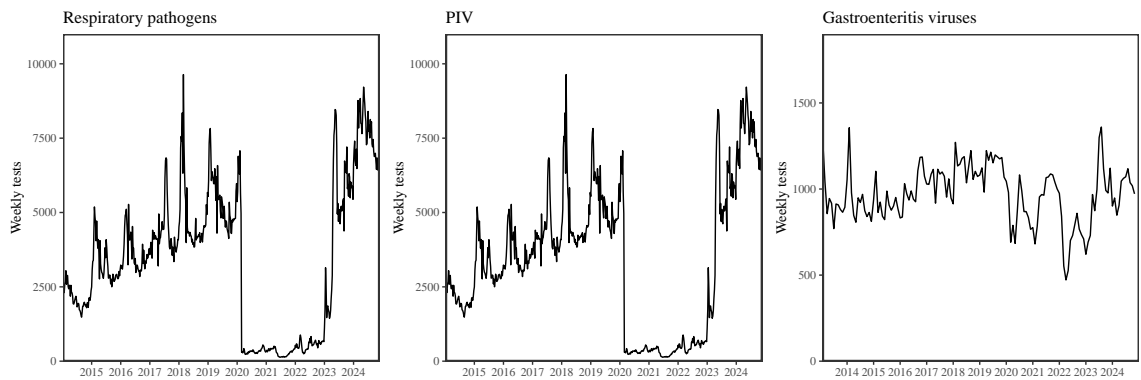


Figure S18: Testing patterns for respiratory pathogens, PIV, and gastroenteritis viruses in Hong Kong.

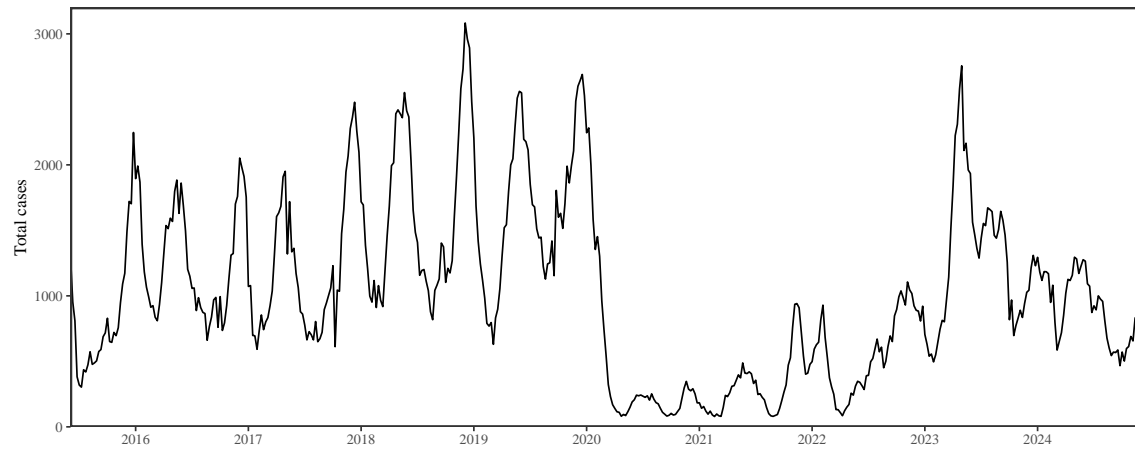


Figure S19: Total number of reported respiratory infection cases in Korea.

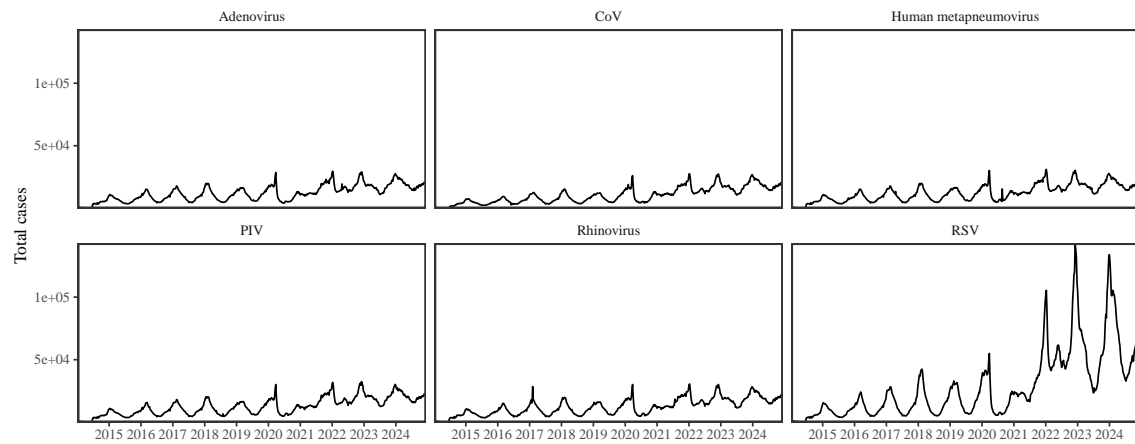


Figure S20: Testing patterns for respiratory pathogens in the US reported through the NREVSS.